MASARYKOVA UNIVERZITA
Přírodovědecká fakulta
Ústav teoretické fyziky a astrofyziky

Bakalářská práce

Brno 2026 Adéla Čuchnová

MASARYKOVA
UNIVERZITA
PŘÍRODOVĚDECKÁ FAKULTA
ÚSTAV TEORETICKÉ FYZIKY A ASTROFYZIKY

Fotometrická studie vybraných hnědých trpaslíků

Bakalářská práce

Adéla Čuchnová

Vedoucí práce: RNDr. Jan Janík, Ph.D. **Brno 2026**

Bibliografický záznam

Autor:	Adéla Čuchnová Přírodovědecká fakulta, Masarykova univerzita Ústav teoretické fyziky a astrofyziky
Název práce:	Fotometrická studie vybraných hnědých trpaslíků
Studijní program:	Fyzika
Studijní obor:	Astrofyzika
Vedoucí práce:	RNDr. Jan Janík, Ph.D.
Akademický rok:	2025/2026
Počet stran:	xiii + 57
Klíčová slova:	hnědí trpaslíci, fotometrie, limit spalování vodíku, zákrytové dvojhvězdy, světelné křivky, barevný index

Bibliographic Entry

Author:	Adéla Čuchnová Faculty of Science, Masaryk University Department of Theoretical Physics and Astrophysics
Title of Thesis:	Photometric study of selected brown dwarfs
Degree Programme:	Physics
Field of Study:	Astrophysics
Supervisor:	RNDr. Jan Janík, Ph.D.
Academic Year:	2025/2026
Number of Pages:	xiii + 57
Keywords:	brown dwarfs, photometry, hydrogen-burning limit, eclipsing binaries, light curves, color index

Abstrakt

Hnědí trpaslíci jsou substelární objekty složené převážně z vodíku, které ovšem nedosahují dostačující hmotnosti potřebné k tomu, aby ve svém jádře dokázaly udržet stabilní jaderné fúze vodíku. Tato práce se zabývá fotometrickou analýzou tří vybraných binárních systémů s předpokládanou přítomností sekundární složky typu hnědého trpaslíka.

Pozorovací data v několika fotometrických filtrech byla získána na Ondřejovské hvězdárně a na hvězdárně Suhora. Redukcí prostřednictvím standardních postupů v softwaru IRAF a aplikací aperturové a diferenciální fotometrie byla získána normalizovaná fotometrická data, z nichž byly pro jednotlivé objekty vykresleny světelné křivky. U dvou zkoumaných objektů byla dále analyzována periodická proměnnost pomocí metody Phase Dispersion Minimization, což vedlo k určení oběžných period daných systémů. Současně byly vypočítány fázově závislé barevné indexy *B*-*V* a analyzovány spektrální energetické distribuce s využitím dat z portálu CDS.

Získané normalizované světelné křivky vykazují charakteristické rysy pro zákrytové dvojhvězdy, jako je zřetelná přítomnost periodických primárních a sekundárních minim. Odvozené periody i proměnnost barevného indexu *B*-*V* jsou v souladu s předpokladem přítomnosti chladné sekundární složky. Ve dvou ze tří zkoumaných případů vykazuje spektrální energetická distribuce infračervený exces, který dodatečně podporuje tvrzení o nízké teplotě sekundární složky. Ve zbývajícím případě se tento trend neprojevil, což je pravděpodobně v důsledku nedostatku dostupných kvalitních měření.

Provedená analýza poskytuje náhled do konfigurace studovaných systémů a svědčí o tom, že všechny tři systémy lze klasifikovat jako téměř kontaktní nebo polodotykové dvojhvězdy se sekundární složkou o nízké hmotnosti, což odpovídá hypotéze o přítomnosti hnědých trpaslíků v těchto systémech.

Tato práce přispívá k charakterizaci binárních systémů založené na pozorování a zároveň ukazuje, že fotometrie, i přes svou relativní nenáročnost, představuje efektivní nástroj pro studium proměnných objektů.

Abstract

Brown dwarfs are substellar objects, composed mainly of hydrogen, that, however, do not have enough mass to sufficiently sustain nuclear fusion of hydrogen in their core. This thesis presents a photometric study of three selected binary systems with suspected brown dwarf companions.

Observational data in multiple photometric filters were obtained at the Ondřejov Observatory and the Mount Suhora Observatory. Through reductions using standard IRAF pipelines and by implementing aperture and differential photometry, normalized photometric data were acquired and light curves for each target were plotted. Periodic variability of two targets was also analyzed using the Phase Dispersion Minimization method, resulting in the orbital period of each system. Additionally, phase-dependent B-V color indices were derived, and spectral energy distributions were examined, making use of data from the CDS portal.

The normalized light curves exhibit typical characteristics of eclipsing binaries, displaying clear periodic primary and secondary minima. The derived periods and B-V color index variability are consistent with the presence of a cool companion to the main star. In two out of three studied cases, the spectral energy distribution presents an infrared excess further supporting the claim about the low temperatures of the companion object. In the one remaining case this trend was not observed, most likely due to the absence of sufficient quality measurements.

Altogether, the analysis of the results provides insight into the configuration of the studied systems. It suggests that all three studied systems are likely near-contact or semi-detached binaries with low-mass companions, matching the premise of the presence of brown dwarf companions in the selected systems.

This work contributes to the observational characterization of binary star systems and demonstrates the usefulness of photometry, in all its relative simplicity, in studying variable objects.

MUNI
SCI

MASARYKOVA UNIVERZITA
PŘÍRODOVĚDECKÁ FAKULTA
KOTLÁŘSKÁ 2, 611 37 BRNO
IČ: 00216224
DIČ: CZ00216224

ZADÁNÍ BAKALÁŘSKÉ PRÁCE

Akademický rok: 2025/2026

Ústav:	Ústav teoretické fyziky a astrofyziky
Studentka:	Adéla Čuchnová
Program:	Fyzika
Specializace:	Astrofyzika

Ředitel *ústavu* PřF MU Vám ve smyslu Studijního a zkušebního řádu MU určuje bakalářskou práci s názvem:

Název práce:	Fotometrická studie vybraných hnědých trpaslíků
Název práce anglicky:	Photometric study of selected brown dwarfs
Jazyk práce:	angličtina

Oficiální zadání:
Student s vlastních naměřených i archviních fotometrických dat určí parametry drah třech vybraných hnědých trpaslíků a pokusí se z O-C diagramu nalézt či vyvrátit přítomnost dalšího tělesa v systémech. Vlastní fotometrická měření mohou být provedena na univerzitní observatoři ve Ždánicích, případně na vysokohorské observatoři Suhora ležící v polských Gorcích.

Literatura:
WARNER, Brian D. *A practical guide to lightcurve photometry and analysis*. Edited by Alan W. Harris. New York: Springer, 2006, xiii, 297. ISBN 0387293655.

BUDDING, E. a Osman DEMIRCAN. *An introduction to astronomical photometry*. 2nd ed. Cambridge: Cambridge University Press, 2007, xvi, 434. ISBN 9780521847117.

Vedoucí práce:	RNDr. Jan Janík, Ph.D.
Datum zadání práce:	16. 10. 2025
V Brně dne:	5. 5. 2026

Zadání bylo schváleno prostřednictvím IS MU.

Adéla Čuchnová, 13. 11. 2025
RNDr. Jan Janík, Ph.D., 23. 11. 2025
RNDr. Luboš Poláček, 11. 12. 2025

Poděkování

Ráda bych poděkovala vedoucímu této bakalářské práce, doktoru Janu Janíkovi za jeho rady, vedení a trpělivost během celého procesu. Díky patří rovněž Astronomickému ústavu Akademie věd České republiky v Ondřejově za možnost využití Perkova dalekohledu k získání dat zpracovávaných v této práci.

Slovy těžko popsatelná vděčnost patří nakonec především mé rodině, přátelům a lásce za bezmeznou podporu a pochopení.

Prohlášení

Prohlašuji, že jsem svoji bakalářskou práci vypracovala samostatně pod vedením vedoucího práce s využitím informačních zdrojů, které jsou v práci citovány.

Brno 13. května 2026 .....

Adéla Čuchnová

Madness, intellect, audacity
Truth and the lack thereof
They will kill us, have no doubt
There are many ways in
But there's only one way out

Before the Fever - Grimes

Contents

Introduction

Nothing in the universe can be said to be irrelevant. From a small atom, to a large black hole, everything matters, everything is deserving of study. This applies to brown dwarfs as well, to which this thesis is dedicated.

Despite the fact that some might rule them out as insignificant due to their small sizes, low temperatures and negligible luminosities, they are no less interesting than anything else found in the universe.

Brown dwarfs are teetering on the borderline between stars and planets. With masses insufficient to sustain stable hydrogen burning, they represent an important class of objects whose physical properties and evolution significantly differ from both main sequence stars and planets. As such, they play a significant role in helping us understand star formation and evolution, binary evolution and primarily the lower limits of stellar structure.

The first part of this thesis focuses on the theory of brown dwarfs. Starting with the history of brown dwarfs and their first discovery, continuing on to the definition of brown dwarfs themselves, explaining what makes them not so stellar anymore and giving insight into electron degeneracy which governs many of their properties. A lot of attention is given to the formation of brown dwarfs, illustrating multiple possible processes through which brown dwarfs can be formed. The evolution and final stages of brown dwarfs are also briefly discussed.

The second part of this thesis then moves on to the practical study of three selected binaries with a suspected brown dwarf companion. Firstly, observations were carried out at the Ondřejov Observatory and at the Mount Suhora Observatory and the acquired data was later reduced and plotted into light curves. For two targets periods and B-V color indices were determined and spectral energy distribution plots were obtained. Detailed interpretation and discussion of all derived results is provided in the Conclusions section.

The aim of this thesis is to shine more light onto the dim world of brown dwarfs, analyze the photometric behavior of the selected targets and assess the evidence for the presence of brown dwarf companions within the systems.

Chapter 1

Brown dwarfs

1.1 The Beginning

The first mentions of brown dwarfs date back to the beginning of the 1960s, when Shiv S. Kumar theorized the existence of, how he called them, ”black” dwarfs (Kumar, 1962). Since central temperature of contracting stars is proportional to M/R and their central density to M/R^3, where M is the mass of the star and R is the radius of the star, he realized that for stars with low enough mass, hydrogen-burning thermonuclear reactions will never ignite due to the partial electron degeneracy of the star's gas caused by a slow rise in central temperature and a rapid rise in central density. Even though, the first two papers, in which Kumar discussed his ideas, were rejected upon submission to the PASP journal, he went on to present his theory and estimations at the 111th meeting of the American Astronomical Society and submitted two new papers to the Astrophysical Journal, both of which were this time accepted and published. After that, many other researchers carried out numerical calculations confirming Kumar's conclusions (Kumar, 2003).

The actual name for brown dwarfs came much later than the prediction of their existence. The term ”black” dwarfs, as Kumar initially called them (Kumar, 1963), was unfit, since it was already being used to label theoretical white dwarf remnants cooled to the point of emitting no light. So, a new name had to be introduced. Various authors suggested various names, such as super-Jupiters, extreme red dwarfs or infrared dwarfs, until Jill Tarter used the term brown dwarf in her PhD thesis in 1975, signifying a color somewhere between black and red (Tarter, 2014), the red color originating from the name of red dwarfs, stars with the minimum required mass for hydrogen burning to be possible.

For the observational discovery of brown dwarfs to be made, everyone then had to wait up until the year of 1995 (Joergens, 2014).

1.2 What is a brown dwarf?

Not really a star, not really a planet. They reside somewhere in the in-betweens. Brown dwarfs are substellar objects, composed mainly of hydrogen, that, however, do not have enough mass to sufficiently sustain nuclear fusion of hydrogen in their core (Burrows & Liebert, 1993). This critical mass, also called the hydrogen-burning limit, is approximately 0.075 $M_\odot$ (Jiang et al., 2004). But even though brown dwarfs are in general not capable of

burning hydrogen stably enough to enter the main sequence and go through the motions of stellar evolution, large-mass brown dwarfs ($M \gtrsim 0.06\ M_\odot$) can go through stages of active fusion of deuterium or even lithium (Burrows & Liebert, 1993; Burrows et al., 2001). It is deuterium-burning that determines the lower mass limit for brown dwarfs, approximately $0.013\ M_\odot$ (Chabrier & Baraffe, 2000).

Possible thermonuclear reactions in brown dwarfs therefore are

$$\begin{aligned} p + d &\rightarrow \gamma + {}^3\mathrm{He}, \\ p + {}^7\mathrm{Li} &\rightarrow 2\alpha, \\ p + {}^6\mathrm{Li} &\rightarrow \alpha + {}^3\mathrm{He}, \end{aligned} \tag{1.1}$$

where p is a proton, d is a deuteron, γ is a gamma-ray photon, ^{3}He is a helium-3 nucleus, ^{7}Li and ^{6}Li are lithium-7 and lithium-6 nuclei, and α is an alpha particle (Burrows et al., 2001).

1.2.1 Lithium and deuterium tests

Lithium and deuterium can serve as indicators for determining whether or not an observed object is in fact a brown dwarf.

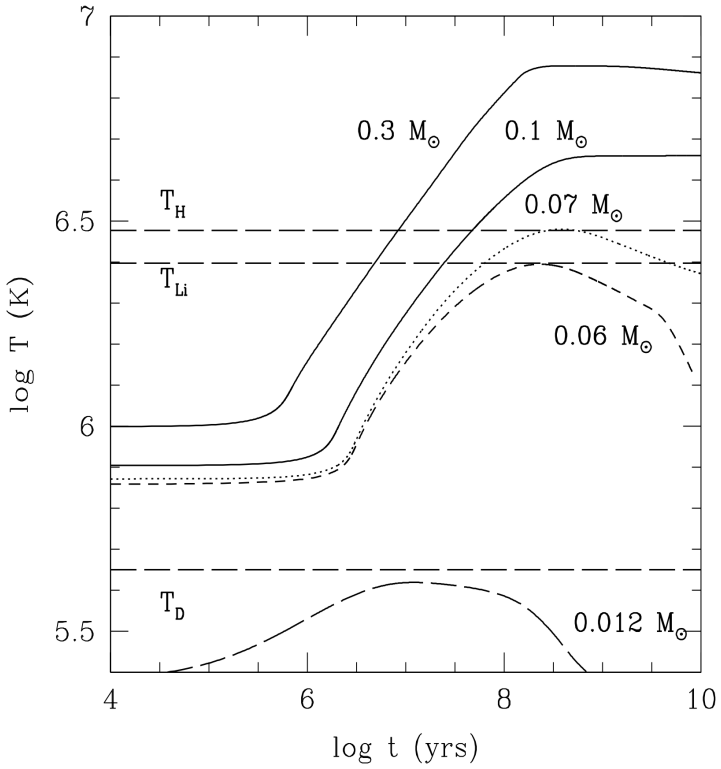

Figure 1.1: Central temperature as a function of age for different object masses. T_H, T_{Li} and T_D indicate burning temperatures of hydrogen, lithium and deuterium, respectively. (Chabrier & Baraffe, 2000)

Lithium burns at central temperatures of around 2.5×10^6 K, which is lower than temperatures required to start hydrogen burning (3×10^6 K (Reid & Hawley, 2005)), and is easily reached even in very low-mass stars. For objects with masses under approximately 0.06 $M_\odot$ the maximum central temperature is always bellow the lithium-burning limit, as is shown in Figure 1.1. (D'Antona & Mazzitelli, 1994; Pozio, 1991) On top of that, lower-mass stars ($M \lesssim 0.5$ $M_\odot$) are fully convective during lithium burning, meaning that in the course of this time span we can assume that their core and atmosphere composition are identical. For low-mass stars it takes about 10^8 years to completely deplete their supply of lithium. (Bildsten et al., 1997)

Therefore, if an observed object is older than 10^8 years and shows a Li I resonance doublet at 670.8 nm in its spectrum, it is very likely to be a brown dwarf. (Chabrier & Baraffe, 2000; Rebolo et al., 1992)

Similarly to lithium, deuterium can also be used to identify brown dwarfs. Deuterium burns at central temperatures of around 0.8×10^6 K (Ventura & Zeppieri, 1998), which is lower than temperatures required to start lithium burning. Thus, deuterium burning happens at even earlier stages and is possible for even lower-mass objects than lithium burning is. For low-mass stars it takes about 4×10^6 years to completely deplete their supply of deuterium. Brown dwarfs with masses larger than 0.02 $M_\odot$ burn through their supply of deuterium in the span of 1×10^6 to 10×10^6 years. (Béjar et al., 1999; Chabrier & Baraffe, 2000)

Therefore, if an observed object is older than 10^8 years, a detection of deuterium signifies a mass lower than the deuterium-burning limit (~ 0.013 $M_\odot$, as is shown in Figure 1.1) and a high likelihood of it being a planet, not a brown dwarf[1].

Although harder to detect than lithium lines, spectroscopic indications of deuterium include absorption lines of deuterated water HDO between 1.2 μm and 2.1 μm (Chabrier & Baraffe, 2000).

[1]Not taking into account formation mechanisms and focusing solely on deuterium-burning limit as a defining boundary between giant planets and brown dwarfs.

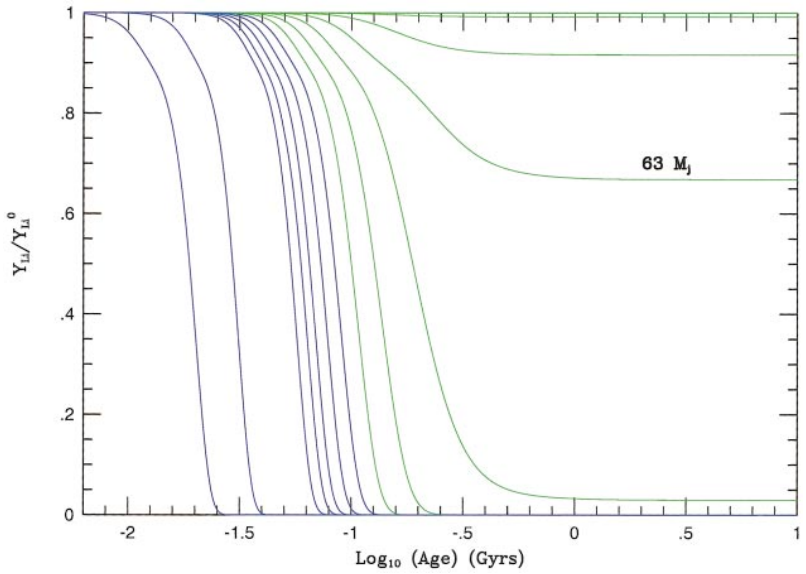

(a) Fraction of initial lithium abundance as a function of age. Objects with the mass of 63 M_J ($\sim 0.06\ M_\odot$) are the lowest-mass objects to burn significant amounts of lithium.

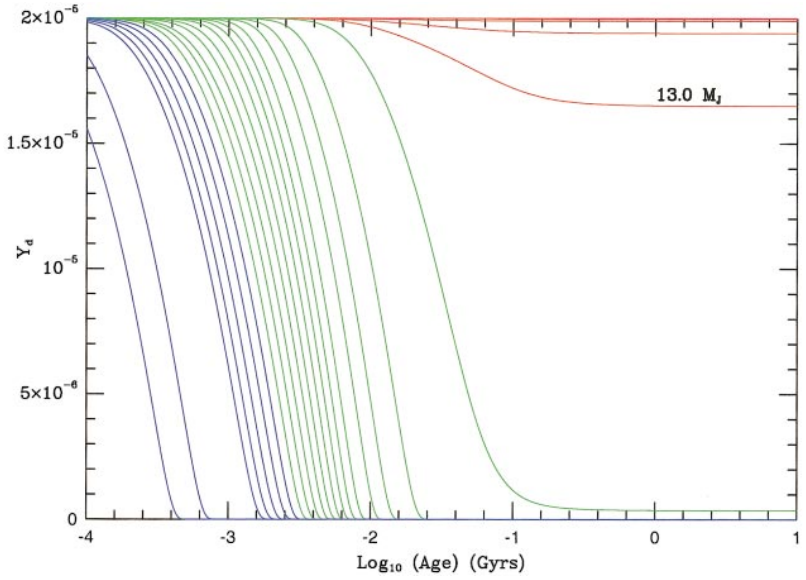

(b) Deuterium mass fraction as a function of age. Objects with the mass of 13 M_J ($\sim 0.012\ M_\odot$) are the lowest-mass objects to burn significant amounts of deuterium. Initial deuterium mass fraction assumed is 2×10^{-5}.

Figure 1.2: Depletion of lithium and deuterium over time, respectively. Stars are shown in blue color, brown dwarfs above 13 M_J are shown in green color, and brown dwarfs and giant planets equal to or bellow 13 M_J are shown in red color. Masses of the objects plotted are 0.3, 0.5, 1.0, 2.0, 3.0, 4.0, 5.0, 6.0, 7.0, 8.0, 9.0, 10.0 11.0, 12.0, 13.0, 15.0 M_J and 0.02, 0.025, 0.03, 0.035, 0.04, 0.045, 0.05, 0.055, 0.06, 0.065, 0.07, 0.075, 0.08, 0.085, 0.09, 0.095, 0.1, 0.15, 0.2 $M_\odot$. (Burrows et al., 2001)

1.2.2 Electron degeneracy

The inability of brown dwarfs to fuse hydrogen is caused by their insufficient mass, which prevents them from ever reaching high enough temperatures required to start up hydrogen-burning thermonuclear reactions.

As stars are born from giant molecular clouds they are contracted by gravity, collapsing on themselves, until their cores become hot enough to ignite nuclear fusion. As hydrogen, and later in stellar evolution heavier elements, burn in the core of a star, gas particles are heated and with received thermal energy are colliding on each other, creating gas pressure. As a result of that, inward gravitational force caused by the mass of the star is balanced out by the outward gas pressure, reaching the state of hydrostatic equilibrium. The equation of hydrostatic equilibrium can be written as

$$\frac{dP(r)}{dr} = -\rho(r)\frac{GM(r)}{r^2}, \tag{1.2}$$

where P is gas pressure, ρ is mass density, G is the gravitational constant, M is mass and r is radius. (Lang, 2013)

For brown dwarfs the situation is different. Just like in main-sequence stars, the core of a newborn brown dwarf keeps heating up as gravity forces it to contract. However, since its mass is too low, its core is not able to reach temperatures high enough for thermonuclear power to balance out the loss of energy through surface radiation before the core becomes electron degenerate and without compensation by compressional heating gradually cools over time, as can be seen in 1.3 (Burrows et al., 2001).

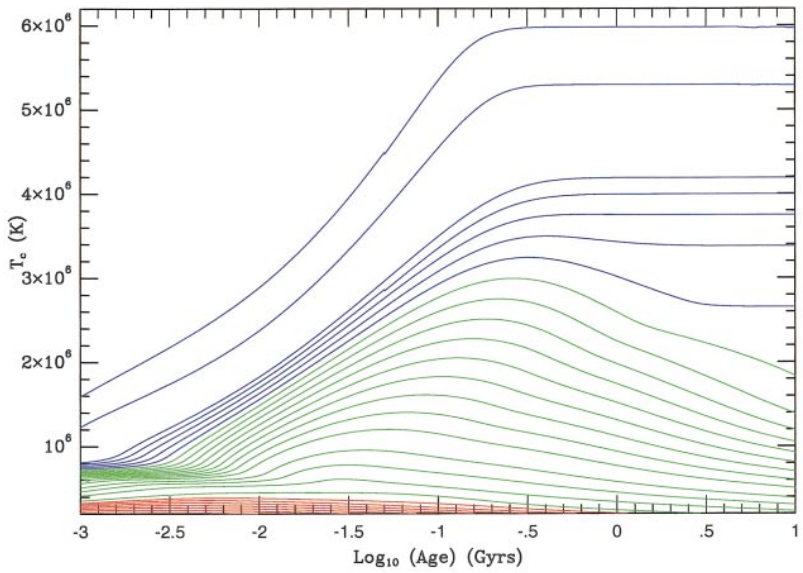

Figure 1.3: Central temperature as a function of age for the same set of objects as in Figure 1.2. (Burrows et al., 2001)

Due to the inability to establish the state of hydrostatic equilibrium gravity keeps on compressing a young brown dwarf further and further. Consequently, central density increases rapidly ($\rho_C \propto M/R^3$) while central temperature, even though also increasing,

rises more slowly ($T_C \propto M/R$) (Kumar, 2003). Because of extremely high densities in the core, gas atoms get so close that they start disrupting the electron shells of one another. At this point, particles start interacting with each other also in between direct collisions and quantum-mechanical effects become relevant.

Temperatures in the core of a brown dwarf are high enough to cause the hydrogen it is composed of to ionize, creating plasma containing both neutral and ionized atoms as well as free electrons. And it is those free electrons that are affected by quantum-mechanical effects most significantly. (Chabrier & Baraffe, 2000; LeBlanc, 2010; Mikulášek & Krtička, 2005)

The Pauli exclusion principle states that no single quantum state can be occupied by two or more identical fermions at once (Altunbulak & Klyachko, 2008). Electrons, having a half-integral spin, are fermions and therefore have to obey this principle.

In consequence of high densities and the Pauli principle, electrons successively fill up all available low-energy quantum states, forcing remaining electrons into higher-energy quantum states. This way, electrons from higher-energy states create electron degeneracy pressure since they cannot be forced into the filled, low-energy states.

When the core of a brown dwarf becomes electron degenerate, contraction is halted as inward gravitational force gets balanced out by the outward electron degeneracy pressure,

$$P_{deg} \sim \rho^{\frac{5}{3}}. \tag{1.3}$$

Thus brown dwarfs are supported by electron degeneracy pressure instead of gas pressure sustained by nuclear fusion as in main-sequence stars. (Oppenheimer et al., 1998)

1.3 Formation of brown dwarfs

Multiple possible processes exist through which brown dwarfs can be formed:

1. turbulent fragmentation,
2. filament fragmentation,
3. disc fragmentation,
4. dynamical ejection,
5. photo-erosion.

None of these mechanisms are mutually exclusive and multiple of them may occur consecutively. (Whitworth & Goodwin, 2005; Whitworth, 2018)

1.3.1 Turbulent fragmentation

Brown dwarfs form by turbulent fragmentation when a supersonic turbulent flow fragments a molecular cloud through highly radiative shock waves, creating high-density regions from which prestellar cores form. Very low-mass prestellar cores then spawn very low-mass

stars, as well as brown dwarfs. (Padoan & Nordlund, 2002; Whitworth & Goodwin, 2005; Whitworth, 2018)

However, there are certain limitations to this formation mechanism. It appears, that brown dwarfs only form when the initial turbulent flow converges from all sides and from relatively small distances (~ 0.02 pc). Turbulent flows such as these occur only occasionally, therefore it seems unlikely that they are sufficiently common to be a dominant formation mechanism for brown dwarfs. (Lomax et al., 2016)

1.3.2 Filament fragmentation

Molecular clouds are not homogeneous but instead have a filamentary structure which is closely connected to prestellar core formations (Arzoumanian et al., 2011). Networks of long, thin filaments form within molecular clouds. Due to gravitational instability the filaments with the highest densities then gradually divide into a number of prestellar cores (André et al., 2010). Some brown dwarfs may form in the filamentary streams that are feeding matter into the center of these clusters of forming stars.

In order for a brown dwarf to be formed through the process of filament fragmentation, it is necessary that its prestellar core forming in the filamentary stream does not accrete too much extra mass and remains under the hydrogen-burning limit. This is possible thanks to two main reasons.

Firstly, when a newborn brown dwarf arrives into the center of a forming star cluster, there is already plenty of more massive stars formed. Therefore there is less easily accretable material available for the newly incoming brown dwarf to accumulate.

And secondly, brown dwarfs tend to arrive to the center of the cluster with high velocities relative to the cluster. Meaning, that they either pass straight through the cluster, or are thrown out of it with even higher velocities upon dynamically interacting with individual stars in the cluster's center. (Bate et al., 2002; Whitworth, 2018)

1.3.3 Disc fragmentation

When a region of a molecular cloud collapses and star creation begins, material with low angular momentum falls directly onto the protostar and material with high angular momentum forms an accretion disc around it. Brown dwarfs then may form as secondary companions from a protostellar disc of a primary star if the right conditions occur.

There are two main requirements that are necessary for a disc to fragment. Firstly, the protostellar disc has to be massive enough so it can be gravitationally unstable and gravity can successfully overcome thermal pressure and centrifugal pressure. And secondly, a proto-fragment has to be able to sufficiently radiate away compressional energy on a dynamical timescale so the accumulated heat does not halt the fragment collapse.

The occurrence of disc fragmentation is possible only at large radii, in the outer layers of protostellar discs ($R \gtrsim 100$ au (Whitworth & Stamatellos, 2006)), because only at these scales material can cool enough to be able to successfully fragment.

Disc fragmentation often results in the formation of multiple low-mass secondary companions. Dynamical interactions between secondary companions may then lead to a complete ejection of some of them from the disc, while others may be pushed further into

the inner layers of the disc. The ones that happen to be ejected then become free-floating brown dwarfs since, thanks to the ejection, they do not accrete additional matter and remain under the hydrogen-burning limit. On the contrary, fragments that stay in the inner disc of the primary star accrete additional matter from it and likely become hydrogen-burning stars. It is possible for some brown dwarfs to exist in the outer disc of the primary star, however, it is not as probable as the other scenarios. (Stamatellos et al., 2007; Whitworth, 2018)

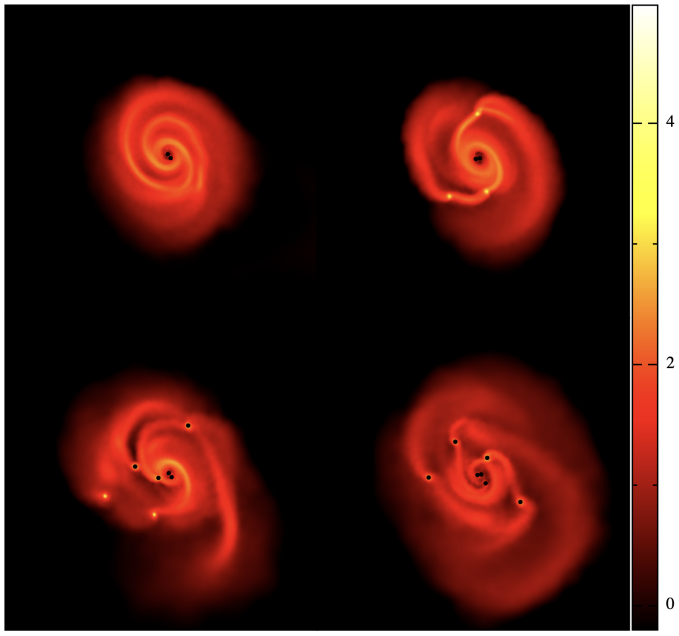

Figure 1.4: A simulation of disc fragmentation in a collapsing prestellar core. Individual frames are at times $t = 59, 60, 61, 62$ kyrs, and show the formation of five brown dwarfs around a close binary system. The disc is approximately 300 au in diameter. The color bar shows the column-density in g.cm^{-2}. (Whitworth, 2018)

1.3.4 Dynamical ejection

When a star formation process is aborted before a prestellar core accumulates enough mass to eventually start up hydrogen burning, it becomes a brown dwarf. What stops them from reaching the hydrogen-burning limit mass is an ejection from their birth clusters due to dynamical interactions with other newborn stars in the cluster. (Reipurth & Clarke, 2001; Whitworth, 2018)

A collapse of a prestellar core is unlikely to spawn only one singular star. Instead, prestellar cores usually form a small cluster of multiple protostars (e.g. Hubber and Whitworth (2005) suggest that the number of born protostars is between 2 and 6, needless to say, the actual number always depends on initial conditions). Individual protostars then grow by competitive accretion and interact dynamically. (Bonnell et al., 1997; Whitworth & Goodwin, 2005)

There are two main scenarios that lead to brown dwarfs creation through dynamical ejection. First possibility is, that the supposed-to-be brown dwarf gets, as a consequence

of dynamical interactions between protostars, promptly ejected from its birthplace. That is, on a timescale shorter than the lifetime of the prestellar core ($\sim 10^5$ years). This means, that the protostar escapes the prestellar core before the accretion process has concluded, and before it has acquired too much mass to surpass the hydrogen-burning limit. (Reipurth & Clarke, 2001)

In the second scenario, the main role is played by competitive accretion. Individual protostars accrete mass at different rates, depending on their position in the gravitational potential of the cluster. Protostars that are at the bottom of the gravitational potential well of the cluster have ample amounts of material at their disposal and can therefore eventually become large stars. On the other hand, protostars that are on the outskirts of the cluster are low in mass and tend to stay that way due to limited amounts of material available. Even though, in this scenario, the supposed-to-be brown dwarf does not have to get ejected in order to retain its low-mass, it will most likely eventually undergo a dynamical interaction with other protostars, that will cause it to escape the cluster completely. (Bonnell et al., 1997; Reipurth & Clarke, 2001; Whitworth, 2018)

The main difference between these two scenarios is the ejection velocity of the brown dwarf. In the first case the expected velocities are an order of magnitude greater than in the second case (Whitworth (2018) suggests an order of $\sim 3\,\mathrm{km.s^{-1}}$ and $\sim 0.3\,\mathrm{km.s^{-1}}$, respectively). (Reipurth & Clarke, 2001)

1.3.5 Photo-erosion

If a prestellar core finds itself in the proximity of a OB star it may become a free-floating brown dwarf or even a planetary-mass object due to the ionizing radiation coming from the OB star (Whitworth & Zinnecker, 2004).

Massive stars inside giant molecular clouds ionize the gas surrounding them because of their high temperatures and create so-called HII regions. Ionization increases the gas temperature (by a factor of ~ 300) in this region and breaks down each hydrogen molecule into a set of two protons and two electrons. This causes an extensive increase in the pressure of the gas (by a factor of order $\sim 10^3$) creating an ionization front which pushes outward into the yet-to-be ionized neutral cloud. (Whitworth, 2018)

Sudden ionization of the surroundings of a prestellar core creates a compression wave which conditions the formation of a protostar in its center. The protostar then begins to grow by accretion. Simultaneously, as the ionization front encounters the prestellar core it begins to eat away at it, removing its outer layers by ionizing them, which causes them to expand away from the center of the core, becoming gravitationally unbound. The final mass of the central protostar is determined by the competition between the rate at which the protostar accretes the infalling envelope and the rate at which the ionization front erodes the envelope.

This formation mechanism is able to operate at a very wide range of conditions and is highly effective in its capability to strip the prestellar core off most of its initial mass. However, its high efficiency coincidentally causes it to be ineffective for brown dwarf production because it requires a relatively massive prestellar core to form a single brown dwarf. (Whitworth & Goodwin, 2005; Whitworth & Zinnecker, 2004; Whitworth, 2018)

1.4 Evolution and the final stage of brown dwarfs

The evolution of brown dwarfs is far less eventful and dramatic than the evolution of hydrogen-burning stars.

When the core of a brown dwarf becomes electron degenerate, contraction is halted and the brown dwarf enters a state of hydrostatic equilibrium supported by electron degeneracy pressure. Since there is no contraction and no hydrogen burning happening, not very much changes after that.

The only signs of evolution in a brown dwarf over time lay in the decrease of temperature and consequential further degeneracy. The brown dwarf eventually ends up almost entirely electron degenerate as it continues indefinitely slowly cooling. Correspondingly to the decrease in temperature its luminosity dims with time, while its radius barely changes. (Mikulášek & Krtička, 2005)

Unlike hydrogen-burning stars, which have multiple possible final stages and endings, brown dwarfs do not really have one at all. All brown dwarfs ultimately evolve into fully degenerate objects with nothing left to bring them back to life. Stranded in space, they are destined to keep on losing heat forever.

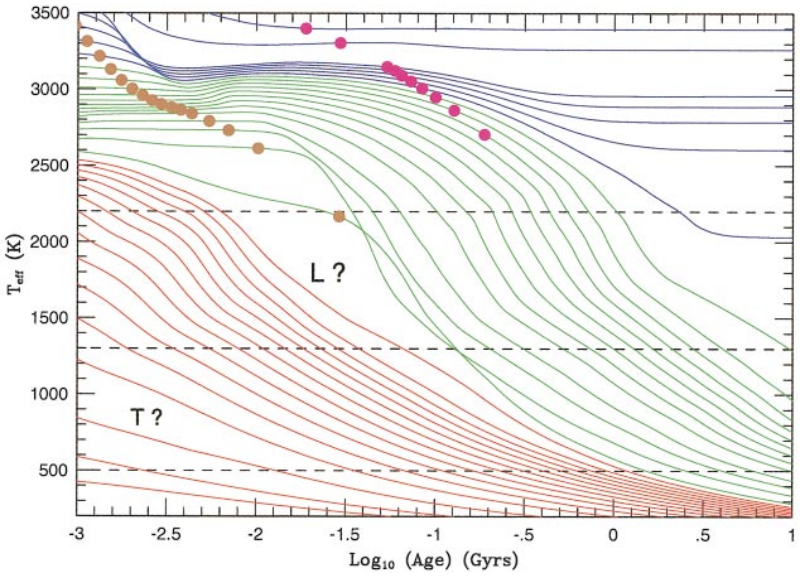

Figure 1.5: Effective temperature as a function of age for the same set of objects as in Figure 1.2. Plotted dots mark the ages for a given mass at which 50% of deuterium (gold) or lithium (magenta) are burned. Approximate realms for L and T spectral type brown dwarfs are indicated by the dashed horizontal lines, spectral type M borders spectral type L on the high-temperature side. (Burrows et al., 2001)

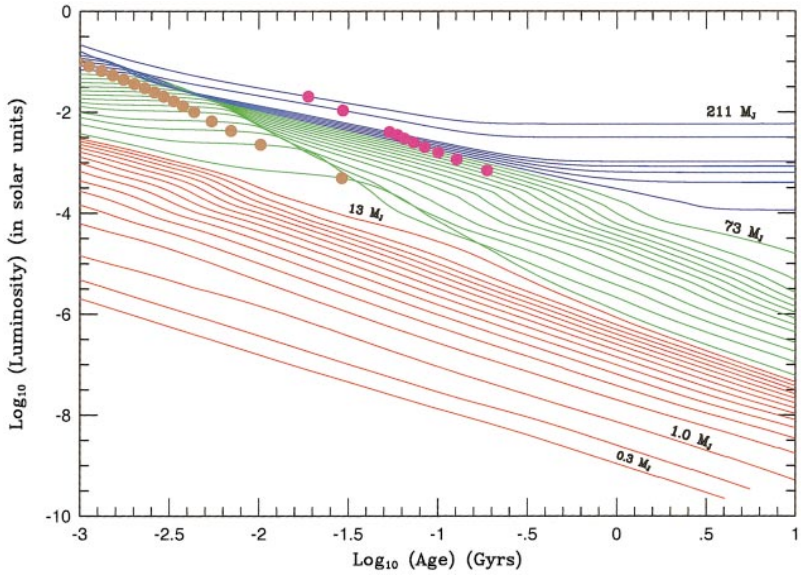

Figure 1.6: Luminosity as a function of age for the same set of objects as in Figure 1.2. Plotted dots mark the ages for a given mass at which 50% of deuterium (gold) or lithium (magenta) are burned. (Burrows et al., 2001)

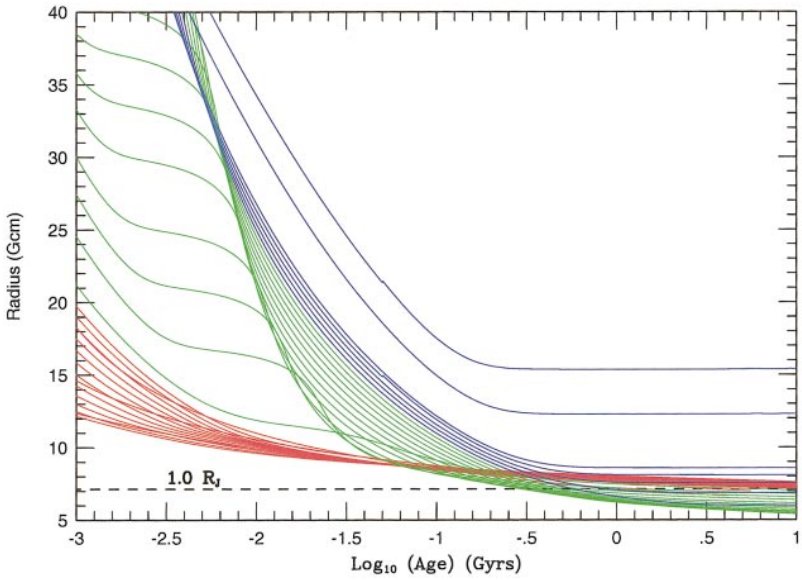

Figure 1.7: Radius as a function of age for the same set of objects as in Figure 1.2. The dashed horizontal line indicates the radius of Jupiter. (Burrows et al., 2001)

1.5 Classification of brown dwarfs

1.5.1 The Morgan-Keenan system

Stars are commonly classified based on the characteristics of their spectrum. The most widely used classification system is the Morgan-Keenan system.

The Morgan-Keenan system consists of three main components:

1. **The spectral type**
   The spectral type classification is determined by the use of seven letters (O, B, A, F, G, K, M) to represent a temperature sequence from hot (O) to cool (M) stars.

Spectral class	Approximate effective temperature [K]
O	31000 – 45000
B	10000 – 31000
A	7300 – 10000
F	5900 – 7300
G	5300 – 5900
K	3900 – 5300
M	2300 – 3900

Table 1.1: Approximate ranges of effective temperatures corresponding to each spectral class. Values listed are based on the works of Pecaut and Mamajek (2013) and have been rounded for clarity.

2. **The luminosity class**
   The luminosity class was originally represented by Roman numbers, added after the spectral type and separated by a space, from I to V, with I being high luminous supergiants and V being less luminous dwarfs. The sequence was eventually expanded on both ends.

Luminosity class	Name
0	hypergiant
Ia	bright supergiant
Ib	supergiant
II	bright giant
III	giant
IV	subgiant
V	dwarf
sd (prefix)	subdwarf
D (prefix)	white dwarf

Table 1.2: Luminosity classes notation (adapted from Gray and Corbally (2009)).

3. **Other characteristics**
   Suffixes or qualifiers can be added to represent other defining characteristics, such as line width, composition anomalies, presence of emission lines, uncertainty in the classification and so on.

1.5.2 Substellar classification

After the discovery of brown dwarfs an extension of the spectral classification had to be made, and thus after the M-type stars now follow three more spectral types (L, T, and Y).

(Apellániz et al., 2024; Gray & Corbally, 2009)

The spectra of these objects have ample of atomic and molecular absorption lines. The most dominant being lines of water, methane, and ammonia. In L and early T type dwarfs, neutral alkali metals and bands of metal oxides and metal hydrides are also present. Just like with the O through M stars, temperature is the major factor for determining the spectral type. (Apellániz et al., 2024; Kirkpatrick, 2005)

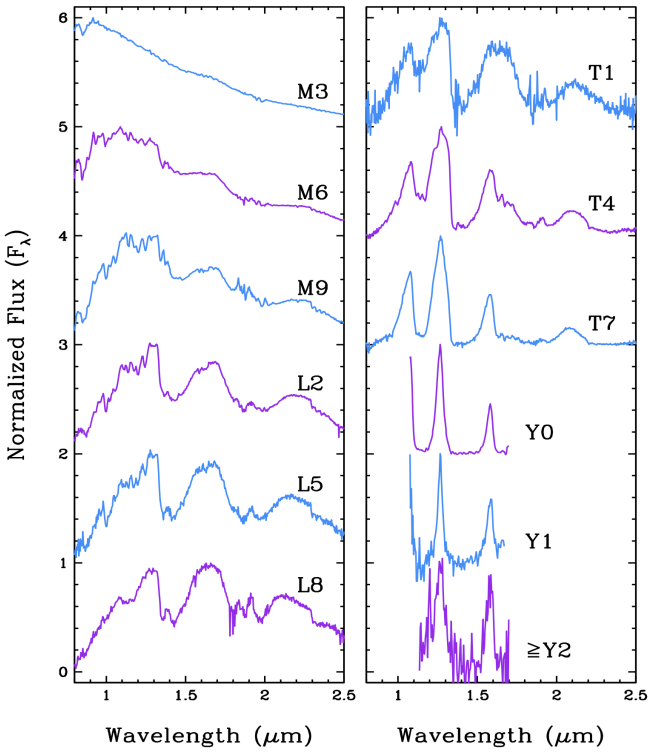

Figure 1.8: The near-infrared spectral sequence from early-M to early-Y types. All spectra are normalized to one at their peak flux and integral offsets are added to the vertical axis to avoid overlaps. (Kirkpatrick, 2013)

Spectral class	Approximate effective temperature [K]
L	1300 – 2300
T	500 – 1300
Y	250 – 500

Table 1.3: Approximate ranges of effective temperatures corresponding to each spectral class. Values listed are based on the works of Pecaut and Mamajek (2013) and have been rounded for clarity.

Surface gravity

Since luminosity classes cannot be applied to LTY dwarfs, surface gravity is used instead for further specification of their classification (Apellániz et al., 2024). However it is

important to note, that gravity classifications are defined primarily for late M-type stars and L-type dwarfs.

Two surface gravity classification systems are implemented:

1. **Optical system** Used for dwarfs with gravity-sensitive features in the optical spectrum (Cruz et al., 2009).

Gravity class	Gravity
α	normal field
β	intermediate
γ	very low

Table 1.4: Gravity classes for the optical system.

2. **Near-IR system** Used for dwarfs with gravity-sensitive features in the near-infrared spectrum (Allers & Liu, 2013).

Gravity class	Gravity
FLD-G	normal field
INT-G	intermediate
VL-G	very low

Table 1.5: Gravity classes for the near-IR system.

Chapter 2

Study of selected brown dwarfs

2.1 Target observations

Three targets were selected for practical observations:

1. J018.4128+22.9608,
2. J296.1785+54.8285,
3. J331.6658+32.7267.

First observations were carried out in 2024 at the Ondřejov Observatory in Ondřejov, Czech Republic as a part of the annual international Workshop on Observational Techniques hosted by the Stellar Department at the Astronomical Institute of the Czech Academy of Sciences in collaboration with the Stellar Astrophysics Group at the University of Potsdam and Thuringian State Observatory.

Later on, in 2026, additional observations were carried out for the purposes of this bachelor's thesis at the Mount Suhora Observatory in the Gorce Mountains, Poland.

2.1.1 Ondřejov Observatory

The Ondřejov Observatory was founded on January 21st 1898 by Josef Frič who set out to honor his and his deceased brother's lifelong goal of building a proper Czech observatory. In 1928, Josef Frič offered his observatory to the state of Czechoslovakia for the purposes of the Charles University which managed it until 1952 when the Czechoslovak Academy of Sciences took over. Today, the observatory is governed by the Astronomical Institute of the Czech Academy of Sciences.

In 1967 an important expansion was made to the observatory in the form of a 2-meter telescope, later named the Perek telescope after the Czech astronomer Luboš Perek. With its 2-meter main mirror, it is the largest telescope in the Czech Republic to this day. The focal length is 29 meters in the Cassegrain configuration and 64 meters in the Coudé configuration. (Suchan, 2018)

2.1.2 Mount Suhora Observatory

In 1983 Professor Jerzy M. Kreiner proposed an idea of building a modern Polish astronomical observatory in a mountainous region with good climatic conditions. After the site selection at Mount Suhora in the Gorce Mountains, construction began in 1986, and the observatory was officially opened in 1987. The Mount Suhora Observatory is operated by the Pedagogical University of Kraków.

The observatory's main astronomical instrument is a 60-centimeter reflecting telescope with a CCD mounted at the primary focus. The focal length of the main mirror is 2.4 meters. (Pedagogical University of Kraków, 2022)

2.1.3 Selected targets

In this section are listed all selected targets, including the filters and exposure times used for each of them, along with the corresponding dates of observation.

Ondřejov Observatory

Target	Filter	Exposure	Date observed
J018.4128+22.9608	i'	60 s	27. 8. 2024
J296.1785+54.8285	g'	20 s	27. 8. 2024
	i'	20 s	29. 8. 2024
	r'	20 s	31. 8. 2024
J331.6658+32.7267	i'	60 s	29. 8. 2024

Table 2.1: Ondřejov observations.

Mount Suhora Observatory

Target	Filter	Exposure	Date observed
J018.4128+22.9608	B, V	300 s	18. 1. 2026
		180 s	19. 1. 2026
		180 s	20. 1. 2026
		180 s	21. 1. 2026
J296.1785+54.8285	B, V	300 s	18. 1. 2026
		180 s	20. 1. 2026
		180 s	5. 3. 2026
		180 s	9. 3. 2026

Table 2.2: Mount Suhora observations.

2.2 Data reduction

2.2.1 Aperture photometry

After initial sorting of all raw images, calibration frames were subtracted and aperture photometry was performed using the Image Reduction and Analysis Facility (IRAF) envi-

ronment with the help of various packages.

In aperture photometry, aperture refers to a circle, containing the star, that marks the area in which the flux of the star is measured. This small section of the sky includes the light from the star, as well as the background light of the sky itself which has to be eliminated in order to receive accurate measurements of the star's brightness. The background light in the aperture is estimated through a patch of sky encircling the aperture, called the annulus. (Berry & Burnell, 2005; Dawson, 2024; Kaur & Joshi, 2022)

To obtain the instrumental magnitudes of the main star and three of its comparison stars, the full width at half maximum (FWHM) was measured to determine the aperture and annulus values needed to perform the IRAF photometry tasks. FWHM is the width of a star's intensity profile measured at a level at which the intensity has fallen to half of its maximum value (Berry & Burnell, 2005).

IRAF

The Image Reduction and Analysis Facility (IRAF) is a software system developed by the National Optical Astronomy Observatories (NOAO) for the purpose of reducing and analyzing astronomical data. The IRAF core system provides a selection of image processing tools using a command line interface. Commands are executed to perform functions, with each task having a parameter file that can be modified to affect the output. Additional IRAF software packages can be installed to run under the IRAF environment. (Barnes, 1993)

For the purposes of this study, the following NOAO packages from IRAF were used to obtain the instrumental photometric data:

1. **astutil** – Astronomical utilities package,
2. **digiphot** – Digital stellar photometry package,
    2.1 **daophot** – DAO crowded-field photometry package,
3. **imred** – Image reductions package,
    3.1 **ccdred** – Generic CCD reductions package.

2.2.2 Differential photometry

With acquired instrumental magnitudes of the main star and three of its comparison stars, differential photometry was performed, through the means of a custom Bourne Again SHell (Bash) script, to calculate the relative magnitude of the main star for the purpose of plotting a light curve.

In differential photometry, the magnitude of the variable main star is derived from the difference between its instrumental magnitude and that of the mean instrumental magnitude of several comparison stars. Since the comparison stars are in the same field of view, have the same observation time and are observed using the same filter as the main star, all atmospheric and equipment effects affecting the brightness of the stars are minimized

when the difference between the main star and comparison stars is taken. (Kaur & Joshi, 2022; Warner, 2016)

The Bash script used for this study creates a reference star by combining the instrumental magnitudes and errors of the comparison stars into a weighted mean instrumental magnitude, which is then subtracted from the instrumental magnitude of the main star to get the sought-after differential magnitude. The error is calculated using the rules of propagation of uncertainty. For better visualization, the differential magnitude is then further normalized by subtracting the mean differential magnitude from it.

The obtained normalized magnitudes were then plotted against the Heliocentric Julian Date resulting in the final light curve.

2.2.3 Final photometric data

An excerpt from the final photometric data is presented here.

HJD 2400000+ [d]	Mag [mag]	Err [mag]
60550.49777	-0.05	0.03
60550.50228	-0.00	0.03
60550.50309	-0.03	0.03
60550.50390	0.11	0.03
60550.50471	0.04	0.03
60550.50552	-0.02	0.03
60550.50633	0.02	0.03
60550.50714	-0.07	0.03
60550.50795	0.00	0.03
60550.50876	0.05	0.03

Table 2.3: Photometric data for J018.4128+22.9608 in filter i'.

The full photometric dataset of each studied star is listed in the Appendix.

2.2.4 Photometric results

The normalized light curve of J018.4128+22.9608 in filter i' is shown in Figure 2.1 as an example of the photometric results.

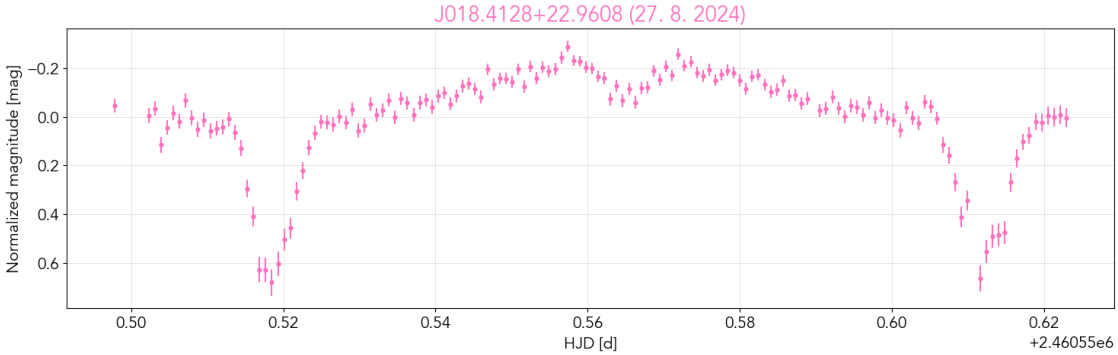

Figure 2.1: Normalized light curve of J018.4128+22.9608 in filter i'.

The normalized light curve of each studied star is shown in the appendix.

2.3 Photometric analysis

As can be seen in the plots from the previous section, data from the Mount Suhora Observatory spans multiple nights with sparser measurements from each night. In order to obtain a more complete light curve it is necessary to first establish the period of the observed photometric variability and then phase-fold the data.

2.3.1 Period determination

The period of the observed photometric variability was determined by Phase Dispersion Minimization (PDM) through a custom Python script.

The PDM technique is an accurate method for determining the period of a dataset in which only a few observations are available, the time intervals are inconsistent, or the light curve is non-sinusoidal (Stellingwerf, 1978).

The Python script used for this study imports a PDM analysis package from PyAstronomy, which scans the data from both B and V filters combined, using a defined search range, and finds the most corresponding frequency. For each trial frequency the data is phase-folded, divided into a designated number of bins inside of which the amount of scatter is measured as theta. The lower the theta value is, the better period alignment does the frequency corresponding to it provide. The period is calculated as an inversion of the best found frequency value. The error is estimated by using a Monte Carlo method with 200 realizations, in which the magnitude values are perturbed according to their uncertainties and the period is recalculated for each realization. The standard deviation of the resulting distribution is then adopted as the error estimate.

The PDM periodogram of J018.4128+22.9608 is shown in Figure 2.2. The best found period is 0.18687 ± 0.00004 days. However, this value corresponds to an alias at twice the actual period. The true period of J018.4128+22.9608 is therefore 0.09344 ± 0.00002 days.

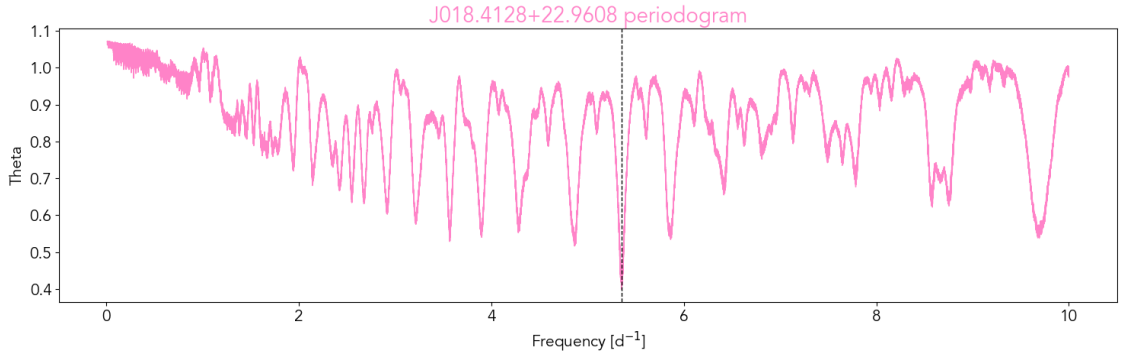

Figure 2.2: Periodogram of J018.4128+22.9608.

The PDM periodogram of J296.1785+54.8285 is shown in Figure 2.3. The best found period is 0.128325 ± 0.000004 days. However, this value corresponds to an alias at twice the actual period. The true period of J296.1785+54.8285 is therefore 0.064163 ± 0.000002 days.

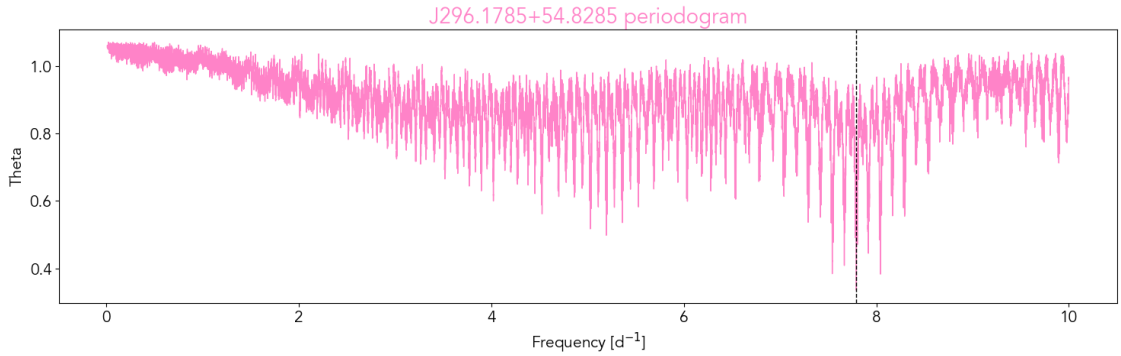

Figure 2.3: Periodogram of J296.1785+54.8285.

To enable the possibility of future minima predictions a linear ephemeris was constructed as

$$T_p = M_0 + PE, \tag{2.1}$$

where T_p is the predicted time of the minimum, M_0 is the reference time of a selected minimum, P is the adopted period and E is the epoch.

The value of the reference time M_0 was determined by fitting a Gaussian function to the primary minimum in the phase-folded light curve. The fitting process is explained more in detail in the following section. The uncertainty of the reference time M_0 corresponds to the uncertainty of the center of the Gaussian fit, which is provided by the Gaussian covariance matrix, converted from phase to time using the period.

The ephemeris of J018.4128+22.9608 is

$$T_p = 2461062.2039(1) + 0.09344(2)E. \tag{2.2}$$

The ephemeris of J296.1785+54.8285 is

$$T_p = 2461061.6628(1) + 0.064163(2)E. \tag{2.3}$$

2.3.2 Phase-folding

Phase-folding was performed with a custom Python script which takes the adopted photometric period and calculates the phase as

$$\phi = \left(\frac{t - t_0}{P} \right) \bmod 1, \tag{2.4}$$

where t is the Heliocentric Julian Date, t_0 is the epoch (here set to the time of the primary minimum) and P is the period.

An estimate of t_0 is made by taking the time of the maximum magnitude data point as an approximate reference time of the primary minimum. Using the estimated t_0 the light curve is provisionally phase-folded to place the primary minimum near phase 0. A Gaussian function is then fitted to the data points surrounding phase 0 in the provisionally phase-folded light curve to more accurately estimate the center of the primary minimum and align it with phase 0. The center of the Gaussian fit gives a phase offset value which is then converted to time and applied as a correction to the previous t_0 estimation.

The final phase-folded light curve is folded with the redefined t_0 value and plotted in two cycles for better visualization as normalized magnitude against the calculated phase.

The phase-folded light curve of J018.4128+22.9608 is shown in Figure 2.4.

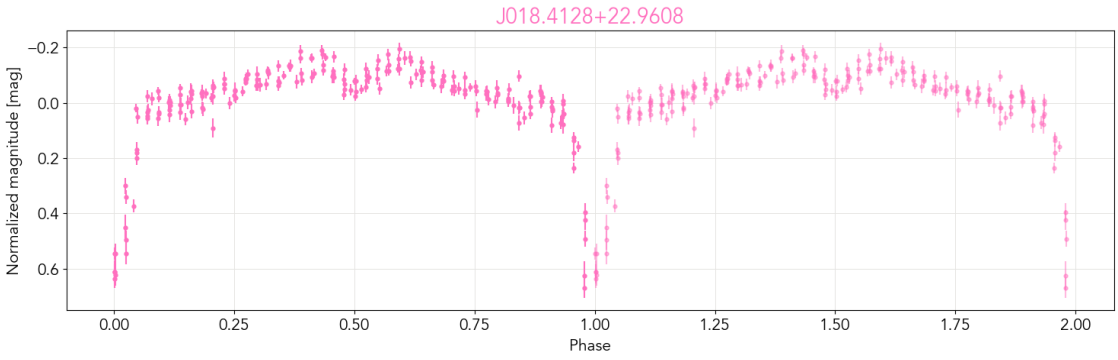

Figure 2.4: Phase-folded light curve of J018.4128+22.9608.

The phase-folded light curve of J296.1785+54.8285 is shown in Figure 2.5.

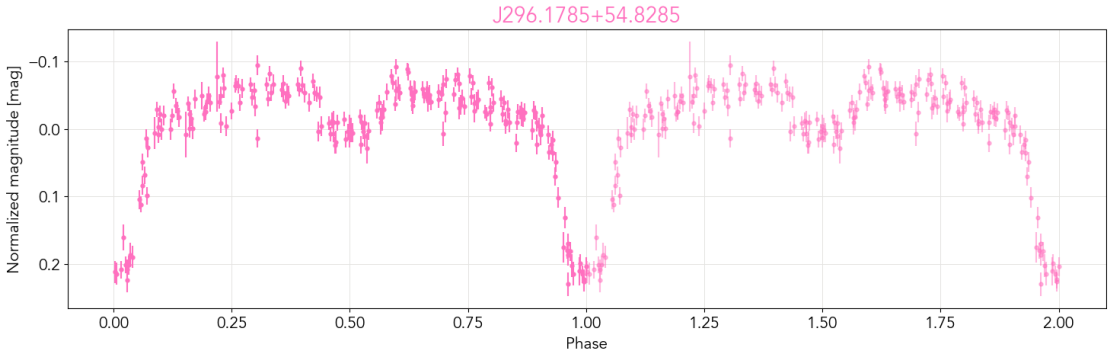

Figure 2.5: Phase-folded light curve of J296.1785+54.8285.

2.3.3 *B-V* color index

Since observations of J018.4128+22.9608 and J296.1785+54.8285 from the Mount Suhora Observatory were carried out in both B and V filters, the possibility of plotting a phase-folded color index presents itself.

A color index is the difference between the magnitudes of a star measured in two different filters. By calculating the color index it is possible to quantify the star's color, and therefore temperature as well. A positive color index signifies a redder, thus cooler, star. A negative color index signifies a bluer, thus hotter, star. An A0 star (e.g. Vega) is used as the zero point of the color index. (Gargaud et al., 2023)

The *B-V* color index was calculated using a custom Python script. Since observations in each filter were not performed at the exact same time it is necessary to first interpolate V-filter magnitudes and errors onto B-filter timestamps. The *B-V* color index is then obtained as

$$B-V = m_B - m_{V_{int}}, \tag{2.5}$$

where m_B is the B-filter magnitude and $m_{V_{int}}$ is the interpolated V-filter magnitude. The decision to interpolate V-filter data onto B-filter data, and not the other way around, was motivated by slightly smaller uncertainties of the B-filter data. The error is calculated using the rules of propagation of uncertainty. The phase-folded color index is then plotted in two cycles for better visualization, as the calculated *B-V* color index against phase. The redefined t_0 value from the Gaussian fit is implemented here in the same manner as during the light curve phase-folding.

It is important to note, that since the *B-V* color index was calculated using normalized differential magnitudes, it does not represent an absolute color index value nor allow for a direct determination of temperature, but rather shows a relative variability with respect to the adopted reference level.

The phase-folded color index of J018.4128+22.9608 is shown in 2.6.

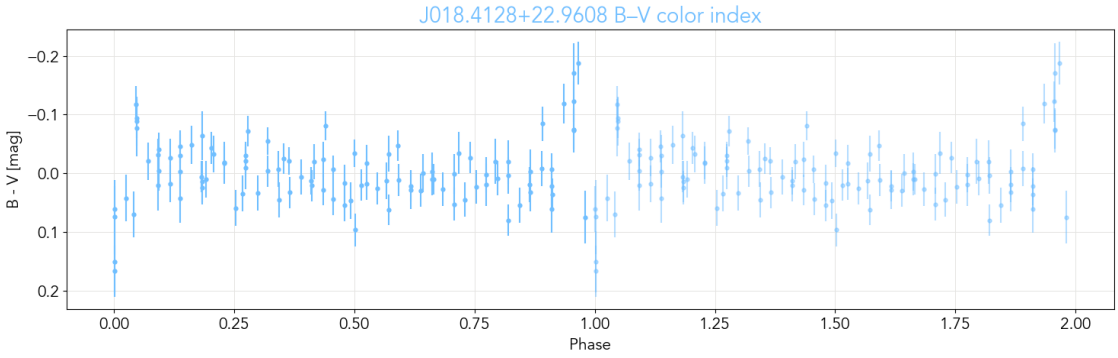

Figure 2.6: Phase-folded color index of J018.4128+22.9608.

The phase-folded color index of J296.1785+54.8285 is shown in 2.7.

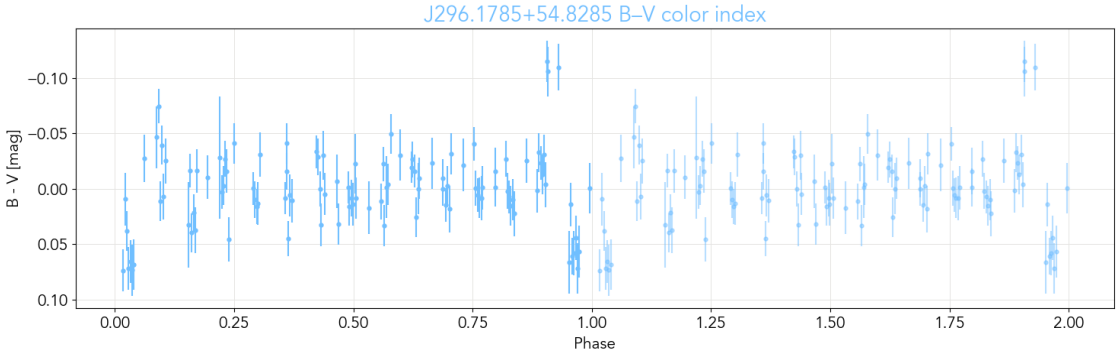

Figure 2.7: Phase-folded color index of J296.1785+54.8285.

2.4 SED

Spectral energy distribution (SED) is a distribution of the source's flux density as a function of frequency or wavelength. Since binary components with unequal temperatures emit flux in different regions of the electromagnetic spectrum, SEDs can be useful for identifying undetermined binaries. The companion star contributes to the SED by influencing the overall flux distribution, possibly manifesting itself as an excess of flux in certain wavelengths corresponding to its temperature. (Jadhav, 2025)

SED data for each target were acquired from the Strasbourg astronomical Data Center (CDS) portal (Wenger et al., 2000).

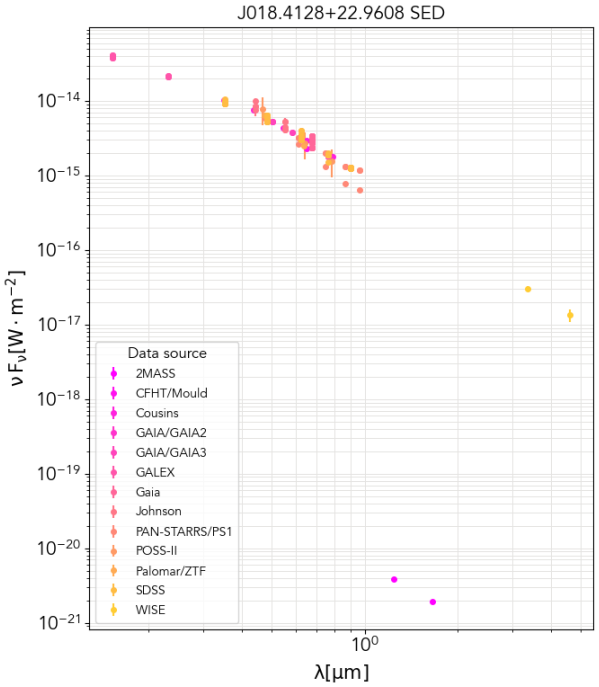

Figure 2.8: Spectral energy distribution of J018.4128+22.9608 with data from the CDS portal (Wenger et al., 2000).

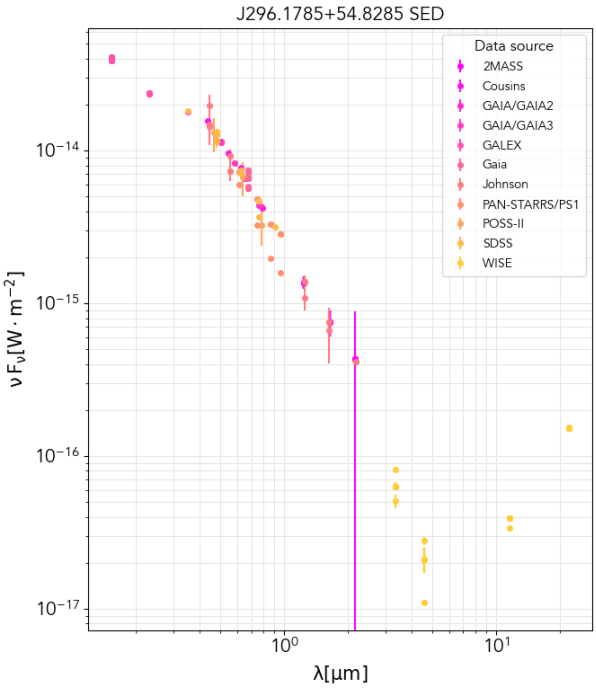

Figure 2.9: Spectral energy distribution of J296.1785+54.8285 with data from the CDS portal (Wenger et al., 2000).

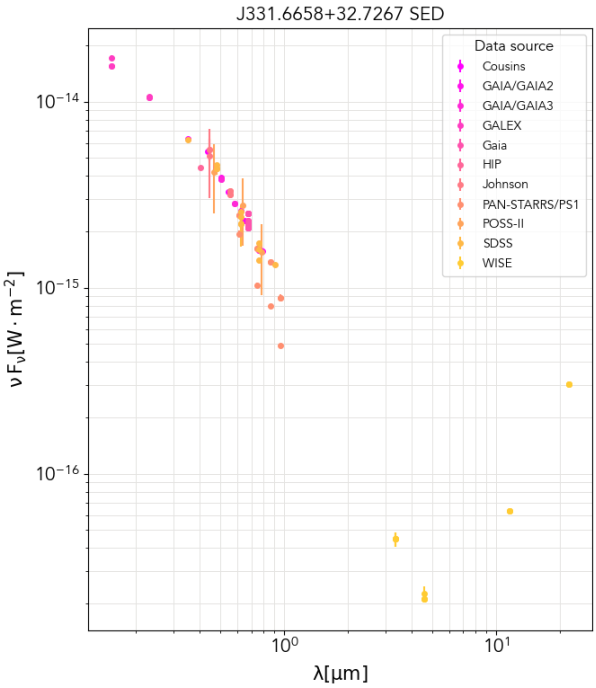

Figure 2.10: Spectral energy distribution of J331.6658+32.7267 with data from the CDS portal (Wenger et al., 2000).

2.5 Conclusions

Observations and photometry were performed on three selected targets.

2.5.1 Data from the Ondřejov Observatory

With data from the Ondřejov Observatory five light curves were obtained (Figures 11 to 15), all clearly displaying characteristic shapes of the primary and secondary minimum, confirming the binary nature of the selected targets.

J018.4128+22.9608

The normalized light curve of J018.4128+22.9608 in filter i' (Figure 11) shows two clear primary minima and one secondary minimum.

The primary minimum is significantly deeper than the secondary minimum, indicating a difference in the effective temperatures of the two components.

The system is likely a near-contact or a semi-detached binary with stars of a tidally distorted shape which is assumed due to the lack of a flat baseline in between eclipses and the short orbital period.

The V-shaped primary minimum indicates a partial eclipse, implying that the inclination of the system is insufficient for a total eclipse to happen. The rounded bottom of the primary minimum is most likely the result of limb darkening of the main star.

J296.1785+54.8285

All three normalized light curves of J296.1785+54.8285 in filters g' (Figure 12), i' (Figure 13) and r' (Figure 14) show a clear primary minimum and a secondary minimum.

In filters g' (Figure 12) and r' (Figure 14) another partial primary minimum and a secondary minimum are visible. However, during both of these observations bad weather and cloud coverage was encountered at the starts and at the ends of the night, resulting in noisier and less precise data, evident especially in the light curve for filter g'.

The primary minima are significantly deeper than the secondary minima, indicating a difference in the effective temperatures of the two components.

A lack of a flat baseline in between eclipses is once again observed, even though less prominent than in the light curve of J018.4128+22.9608 (Figure 11), which together with a short orbital period is a sign of a near-contact or a semi-detached binary with stars of a tidally distorted shape.

The U-shaped primary minima indicate a significant difference in the size of the two components as well as a near edge-on inclination of the system. The rounded bottoms of the primary minima are most likely the result of limb darkening of the main star.

J331.6658+32.7267

The normalized light curve of J331.6658+32.7267 in filter i' (Figure 15) shows a clear secondary minimum and an incomplete primary minimum. During the observations bad

weather and cloud coverage was encountered, resulting in missing data from the primary minimum and noisier and less precise data right after it.

Despite the primary minimum being incomplete, it is evident that it is significantly deeper than the secondary minimum, indicating a difference in the effective temperatures of the two components.

A strong continuous variability in between eclipses can be seen, suggesting a near-contact or a semi-detached binary with stars of a tidally distorted shape.

A near edge-on inclination of the system is assumed from the narrowness of the primary minimum, although this statement cannot be supported by the shape of the bottom of the primary minimum due to missing data.

2.5.2 Data from the Mount Suhora Observatory

With data from the Mount Suhora Observatory sixteen light curves were obtained (Figures 16 to 27). Since the observations from the Mount Suhora Observatory were performed with longer exposures and shorter durations per one night the individual light curves do not have enough data coverage to bear any scientific value on their own, therefore period determination and phase-folding were performed in order to acquire more complete light curves with higher data coverage. In addition, color indices were also plotted.

J018.4128+22.9608

The determined period of J018.4128+22.9608 is 0.09344 ± 0.00002 days. The ephemeris is $T_p = 2461062.2039(1) + 0.09344(2)E$.

The phase-folded light curve (Figure 2.4) confirms all claims derived from the data from the Ondřejov Observatory mentioned in the previous section.

The phase-folded color index (Figure 2.6) shows a clear change of the *B*-*V* color index value at the times of the primary minimum. A prominent spike (corresponding to a decrease in the *B*-*V* color index value due to an inverted y-axis) can be seen at the instance of the beginning of the primary minimum. This phenomenon is caused by the eclipse of the edge of the main star, which exhibits limb darkening, by its companion.

Limb darkening is wavelength dependent, it has a stronger effect at the blue end of the spectrum and a weaker effect at the red end of the spectrum. Therefore, in this case, the eclipse of the limb-darkened edge of the main star causes an increase in observed magnitude that is, relatively to the pre-eclipse value, larger in the *V*-band. This causes the decrease of the *B*-*V* color index which is observed as a spike in the plot. This explanation is further supported by the rounded bottom of the primary minimum present in the light curves, which was discussed in the previous section. Uniform intensity distribution without any limb darkening effects would result in an almost rectangular shape minima with flat bottoms. The limb darkening effect causes the minima to have shallower slopes and a rounded bottom. (Hayek et al., 2012)

Thus in summary, at the beginning of the primary minimum the system's apparent temperature is higher (lower *B*-*V* color index value) than it is out of the eclipse, due to a relatively stronger decrease in the *V*-band flux. For the rest of the duration of the primary minimum, as the hotter main star is transited by its companion, the system's apparent

temperature drops (higher *B-V* color index value) relative to the out-of-eclipse baseline, due to the reduction of the blue-dominated flux from the main star.

J296.1785+54.8285

The determined period of J296.1785+54.8285 is 0.064163 ± 0.000002 days. The ephemeris is $T_p = 2461061.6628(1) + 0.064163(2)E$.

The phase-folded light curve (Figure 2.5) confirms all claims derived from the data from the Ondřejov Observatory mentioned in the previous section.

The phase-folded color index (Figure 2.7) shows a clear change of the *B-V* color index value at the times of the primary minimum. At the beginning of the primary minimum the system's apparent temperature is higher (lower *B-V* color index value) than it is out of the eclipse. For the rest of the duration of the primary minimum the system's apparent temperature drops (higher *B-V* color index value) relative to the out-of-eclipse baseline. The reasoning behind these phenomenons is the same as in the cases discussed in the previous section.

2.5.3 SED

Additional SED plots were acquired with data from the CDS portal.

The SED plots of all three targets show a similar negative slope trend stretching from the ultraviolet, through optical, to near-infrared wavelengths which represents the emission of the photosphere of the main star.

SED plots of J296.1785+54.8285 and J331.6658+32.7267 both exhibit an infrared excess in the form of an upward slope in the infrared wavelengths. This is most likely due to the presence of the much cooler companion star which emits most light in the infrared wavelengths, compared to the main star which is dominant in optical and ultraviolet wavelengths.

However, the SED plot of J018.4128+22.9608 does not show any signs of the infrared excess and displays two outliers in the near-infrared wavelengths. These outliers are presumably faulty data possibly caused by the sensitivity limitations of the Two Micron All Sky Survey (2MASS) by which they were measured by (Skrutskie et al., 2006). The lack of the infrared excess might be explained by insufficient measurements or by the presumption that the companion star is too low-mass or too cool to contribute with any detectable flux to the overall spectral energy distribution.

Summary

This thesis focused on the photometric study of three selected binary systems with suspected brown dwarf companions. The aim of this study was to analyze the results derived from the acquired observational data and be able to confidently rule out or affirm the binary nature of the targets and the existence of their companion objects.

Observations were carried out at the Ondřejov Observatory and at the Mount Suhora Observatory using multiple photometry filters. At the Ondřejov Observatory the observations per one night were of longer duration with shorter exposure times, therefore providing light curves with high density of data points coverage from just one night of observations. On the contrary, at the Mount Suhora Observatory targets were measured in each filter for multiple nights with the observations per one night being of shorter duration with longer exposure times. To acquire the sought-after light curves, the data had to be therefore phase-folded. The orbital periods of the two targets observed at the Mount Suhora Observatory, necessary for proper phase-folding, were determined through the Phase Dispersion Minimization method. Ephemerides were also constructed, with the use of a Gaussian function fit for obtaining the reference time value. The resulting periods and ephemerides are listed here.

Target	Period [d]	Ephemeris
J018.4128+22.9608	0.09344 ± 0.00002	2461062.2039(1) + 0.09344(2)E
J296.1785+54.8285	0.064163 ± 0.000002	2461061.6628(1) + 0.064163(2)E

Table 2.4: Final determined periods and ephemerides of selected targets.

All observations at the Mount Suhora Observatory were for both targets carried out in filters B and V. Thanks to this it was possible to calculate the phase-dependency of the B-V color index.

Additionally, spectral energy distribution plots with data from the CDS portal were included to provide even more information about the studied targets.

From the light curves alone, all three selected targets exhibit clear signs of periodical apparent magnitude variability, displaying distinguishable primary and secondary minima, supporting their classification as eclipsing binaries. Light curves are the fingerprints of variable objects, disclosing information about the target which would otherwise be hard to obtain. Deeper analysis of each light curve is given in the Conclusions section.

The B-V color index further supports what was deduced from the light curves. Clear signs of phase-dependent color index changes and limb darkening are prominent in the phase-folded B-V color index plots. The increase of the B-V color index value gives

evidence to the companion object being of lower temperature than the main star which it orbits.

The spectral energy distribution further testifies to the low temperature of the companion object. Despite the main star dominating most of the SED plot, prevailing in the ultraviolet and optical parts of the spectrum, the SED plots of J296.1785+54.8285 and J331.6658+32.726 exhibit an excess in the infrared part of the spectrum, supporting the hypothesis of the companion being a brown dwarf. The SED plot of J018.4128+22.9608 does not show any signs of the infrared excess which, however, does not altogether deny the existence of the brown dwarf companion in this system.

In conclusion, the discussed results strongly suggest that all three selected targets are near-contact or semi-detached binaries with low-mass companions which may be brown dwarfs. To be able to confidently confirm the companion objects as brown dwarfs further spectroscopic radial velocity measurements and light curve modeling would be required in order to determine the masses of the objects and decide whether or not they fall within the constraints of the hydrogen-burning limit.

Appendix

Appendix A Photometric results from the Ondřejov Observatory

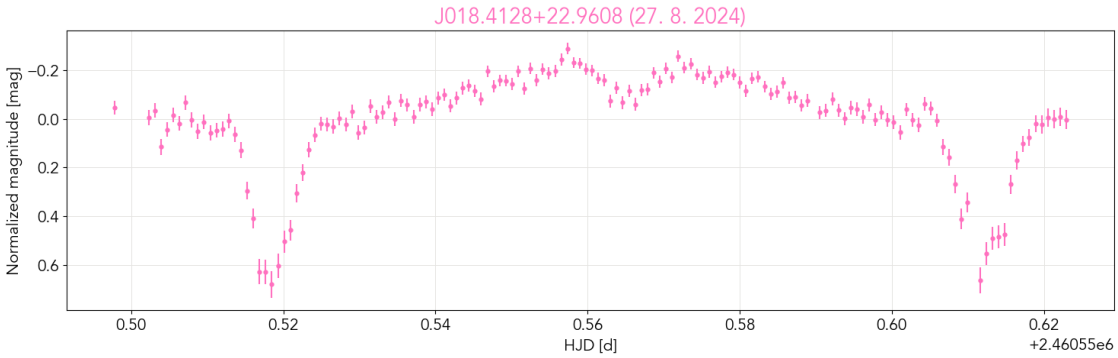

Figure 11: Normalized light curve of J018.4128+22.9608 in filter i'.

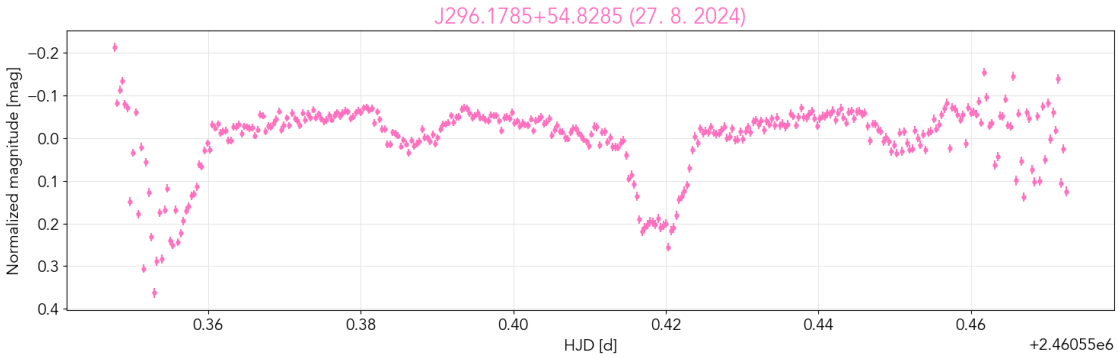

Figure 12: Normalized light curve of J296.1785+54.8285 in filter g'.

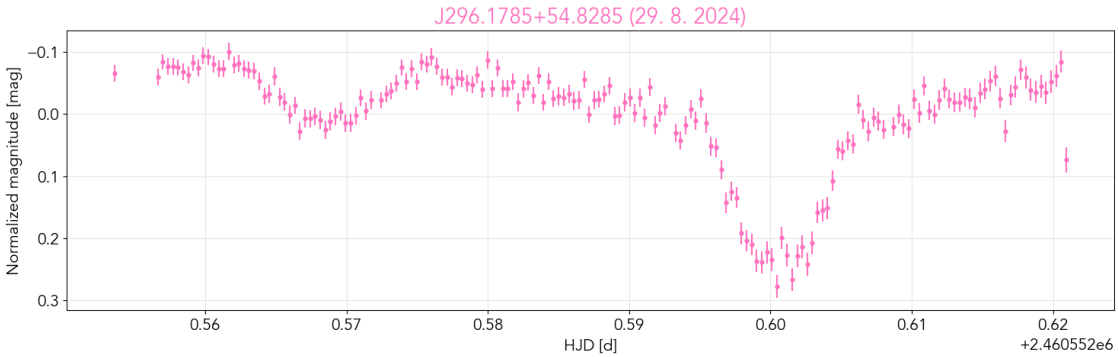

Figure 13: Normalized light curve of J296.1785+54.8285 in filter i'.

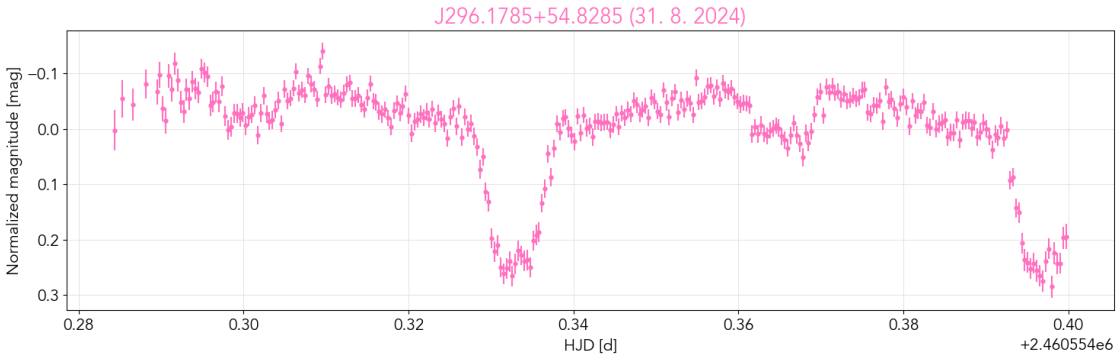

Figure 14: Normalized light curve of J296.1785+54.8285 in filter r'.

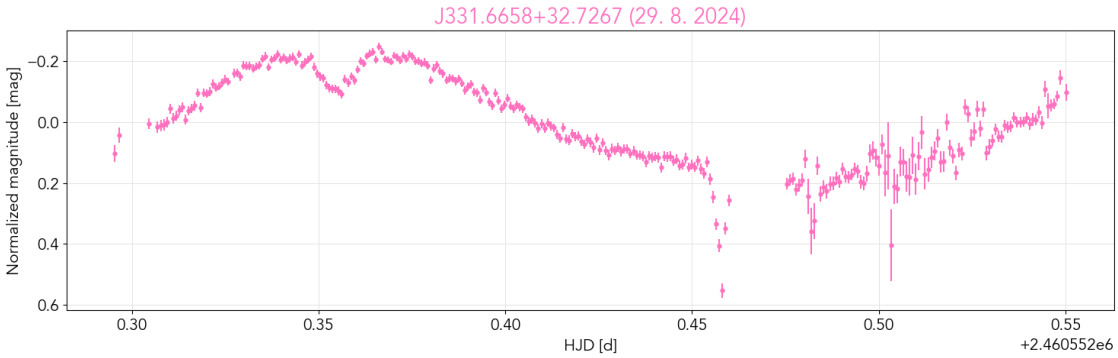

Figure 15: Normalized light curve of J331.6658+32.7267 in filter i'.

Appendix B Photometric results from the Mount Suhora Observatory

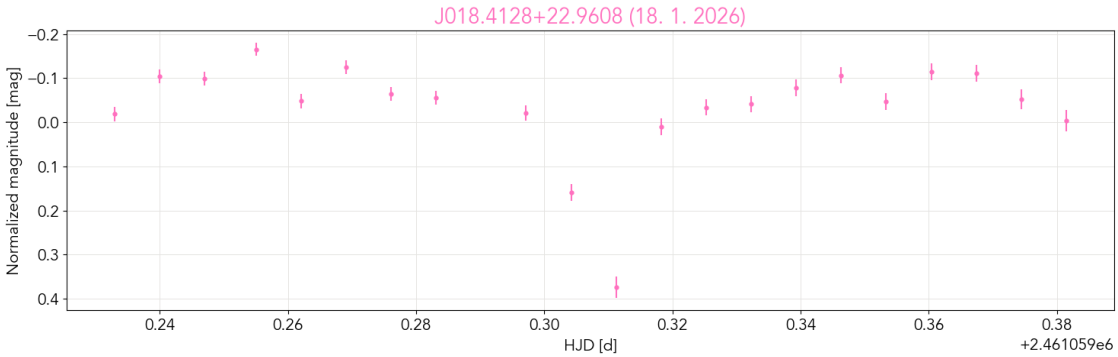

Figure 16: Normalized light curve of J018.4128+22.9608 in filter *B*.

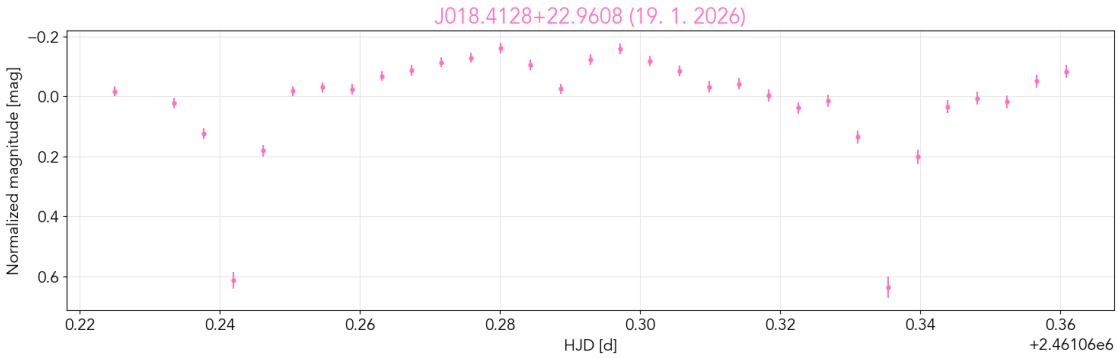

Figure 17: Normalized light curve of J018.4128+22.9608 in filter *B*.

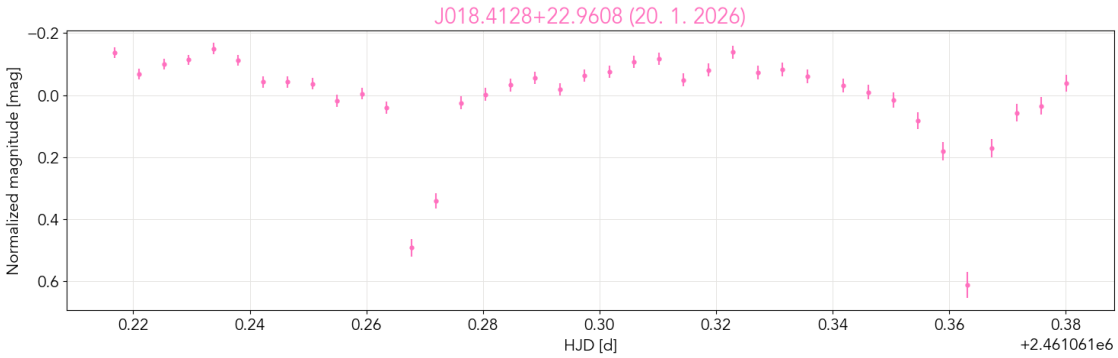

Figure 18: Normalized light curve of J018.4128+22.9608 in filter *B*.

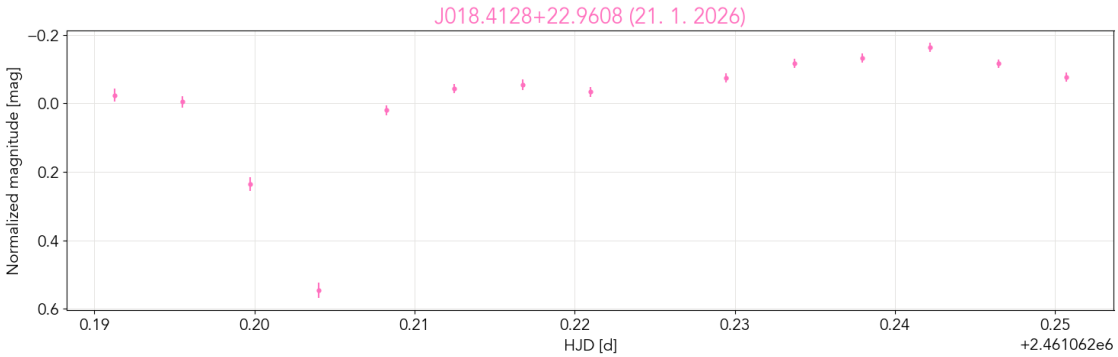

Figure 19: Normalized light curve of J018.4128+22.9608 in filter *B*.

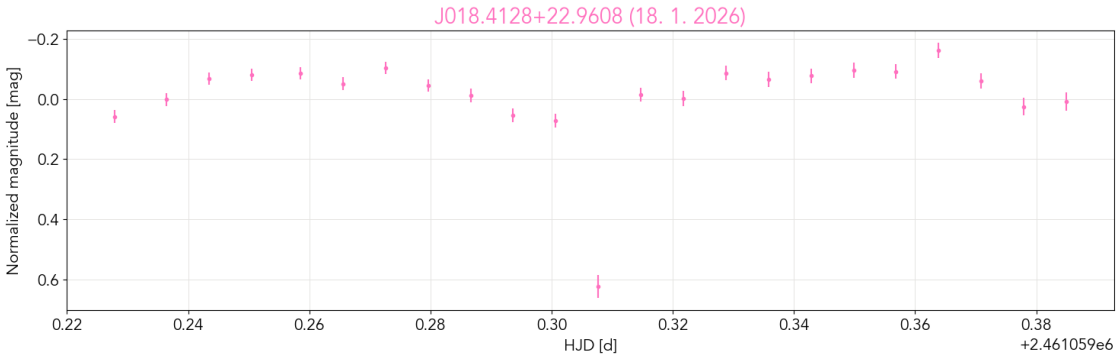

Figure 20: Normalized light curve of J018.4128+22.9608 in filter *V*.

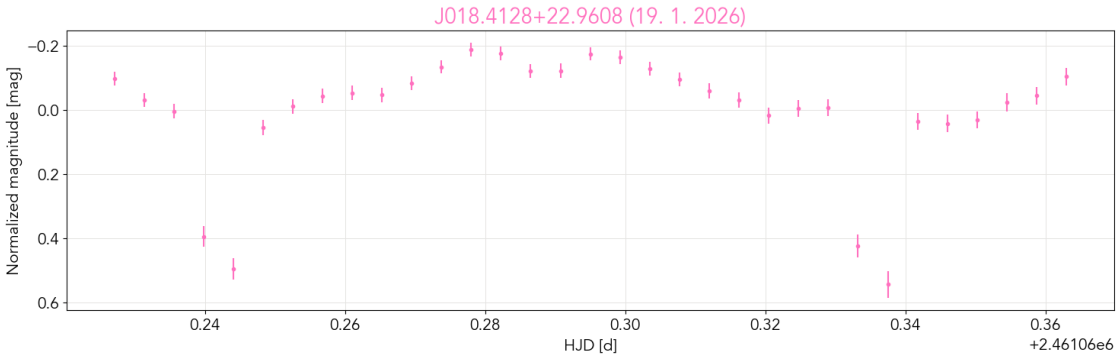

Figure 21: Normalized light curve of J018.4128+22.9608 in filter *V*.

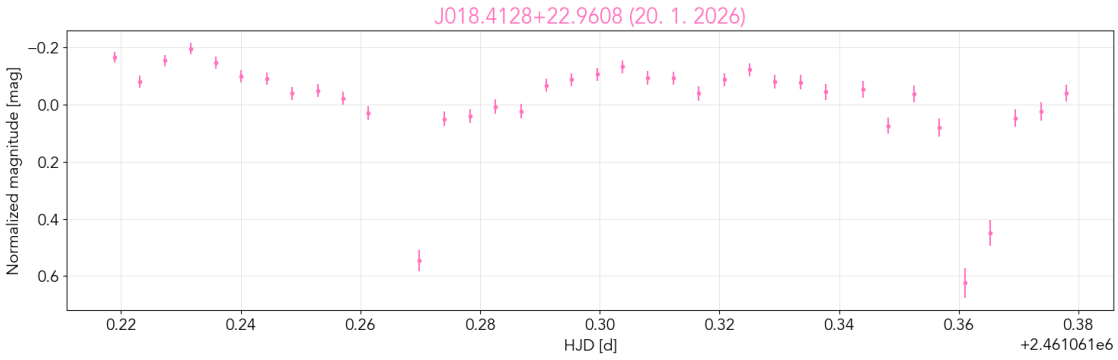

Figure 22: Normalized light curve of J018.4128+22.9608 in filter V.

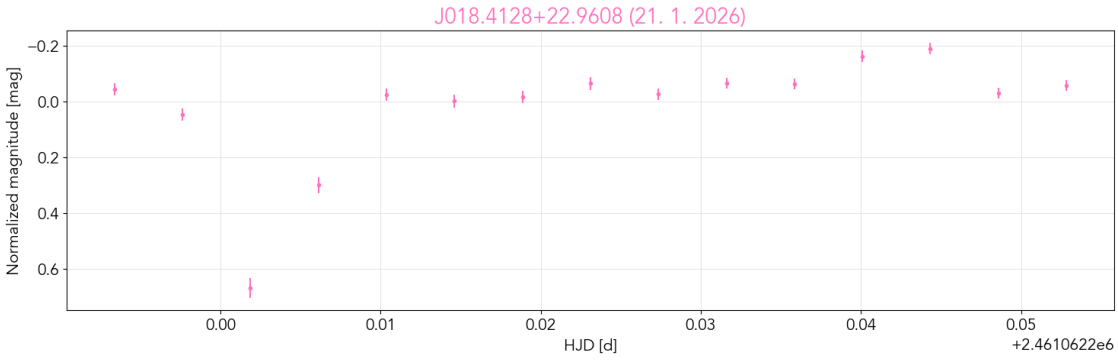

Figure 23: Normalized light curve of J018.4128+22.9608 in filter V.

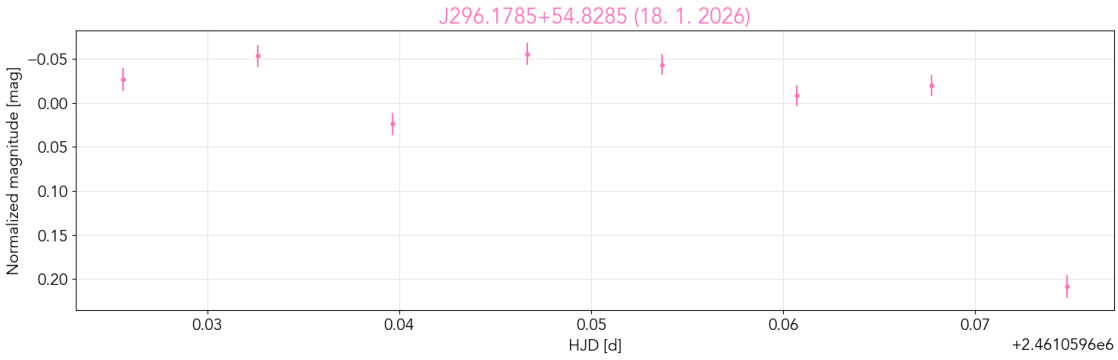

Figure 24: Normalized light curve of J296.1785+54.8285 in filter B.

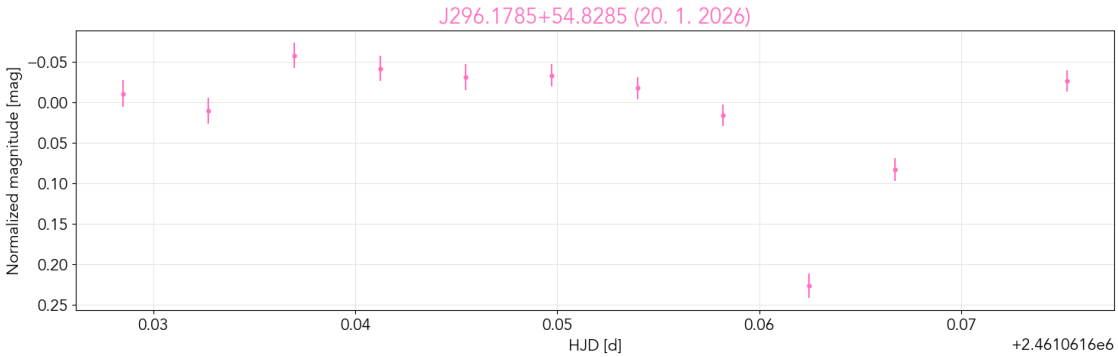

Figure 25: Normalized light curve of J296.1785+54.8285 in filter *B*.

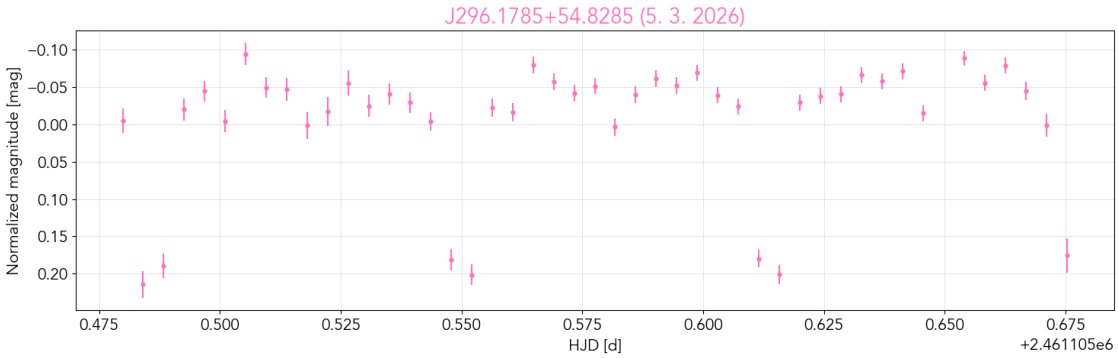

Figure 26: Normalized light curve of J296.1785+54.8285 in filter *B*.

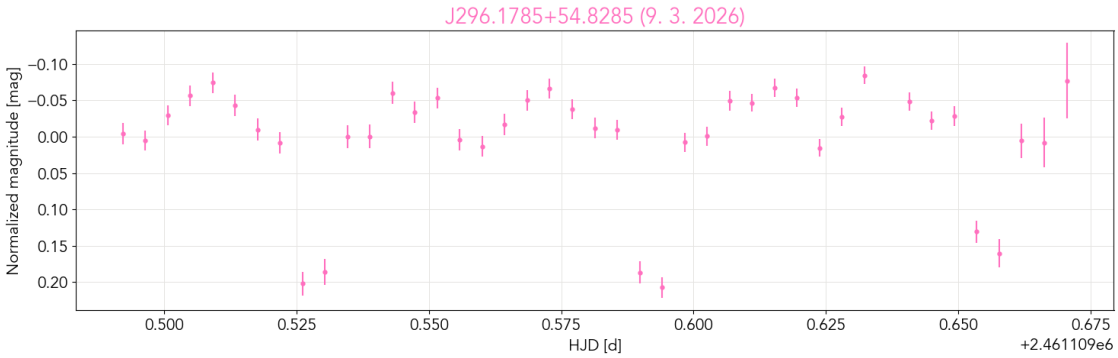

Figure 27: Normalized light curve of J296.1785+54.8285 in filter *B*.

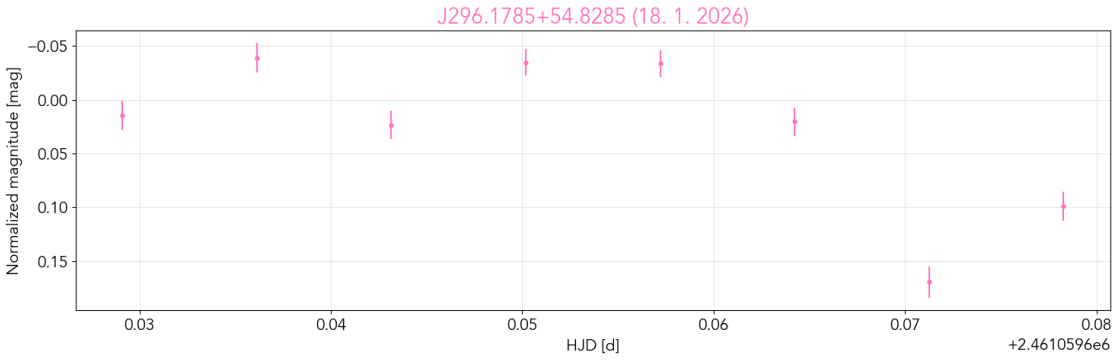

Figure 28: Normalized light curve of J296.1785+54.8285 in filter V.

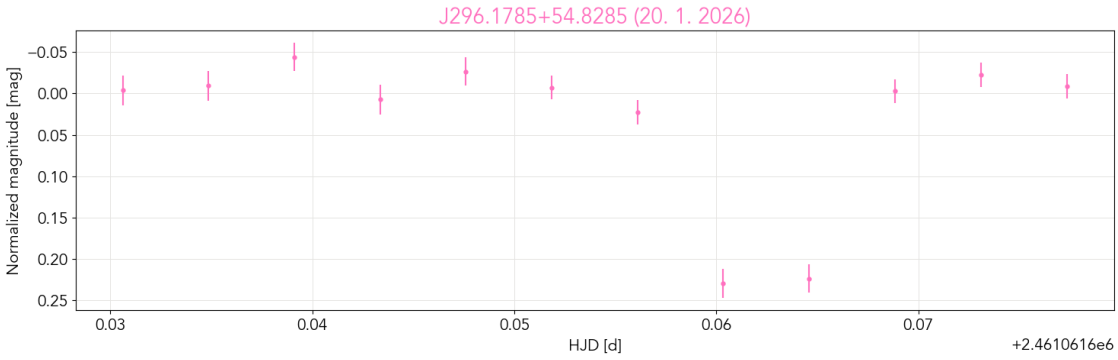

Figure 29: Normalized light curve of J296.1785+54.8285 in filter V.

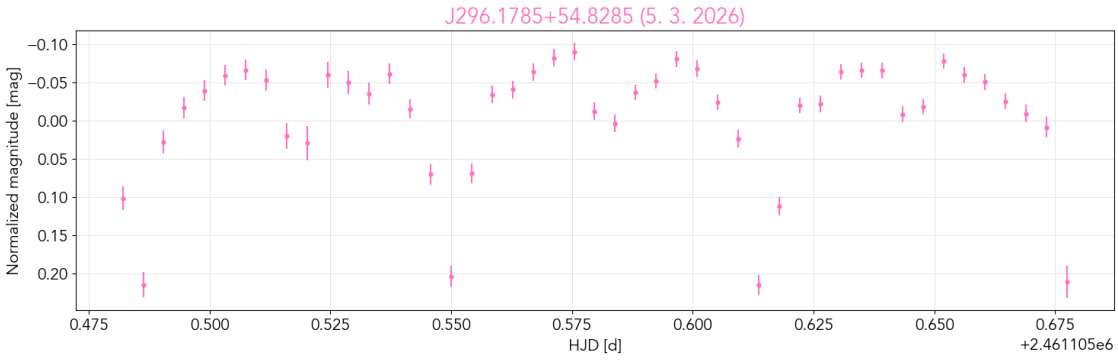

Figure 30: Normalized light curve of J296.1785+54.8285 in filter V.

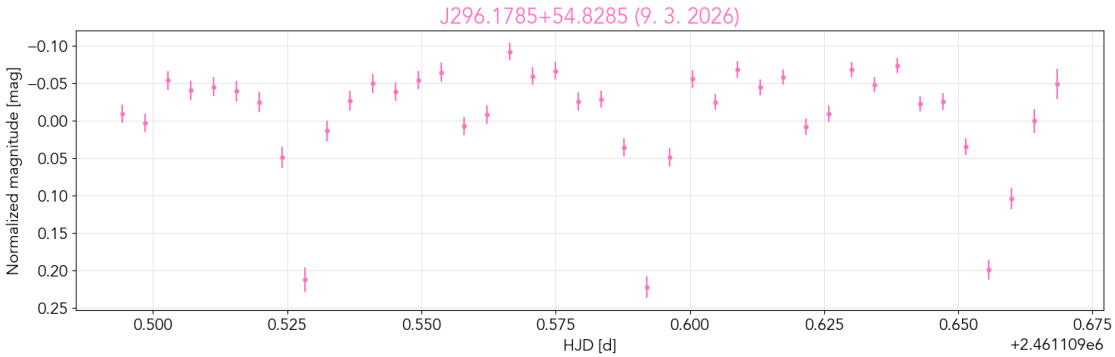

Figure 31: Normalized light curve of J296.1785+54.8285 in filter V.

Appendix C Data from the Ondřejov Observatory

Table 5: Photometric data for J018.4128+22.9608 in filter i'.

HJD 2400000+ [d]	Mag [mag]	Err [mag]	HJD 2400000+ [d]	Mag [mag]	Err [mag]	HJD 2400000+ [d]	Mag [mag]	Err [mag]
60550.49777	-0.05	0.03	60550.54197	-0.05	0.03	60550.58245	-0.17	0.02
60550.50228	-0.00	0.03	60550.54278	-0.09	0.03	60550.58326	-0.13	0.02
60550.50309	-0.03	0.03	60550.54359	-0.13	0.03	60550.58407	-0.10	0.02
60550.50390	0.11	0.03	60550.54440	-0.14	0.03	60550.58488	-0.11	0.02
60550.50471	0.04	0.03	60550.54520	-0.11	0.02	60550.58569	-0.15	0.02
60550.50552	-0.02	0.03	60550.54601	-0.08	0.03	60550.58650	-0.09	0.02
60550.50633	0.02	0.03	60550.54682	-0.20	0.02	60550.58731	-0.09	0.03
60550.50714	-0.07	0.03	60550.54763	-0.13	0.03	60550.58812	-0.06	0.03
60550.50795	0.00	0.03	60550.54844	-0.16	0.02	60550.58893	-0.08	0.03
60550.50876	0.05	0.03	60550.54925	-0.16	0.02	60550.59055	-0.03	0.03
60550.50957	0.01	0.03	60550.55006	-0.14	0.02	60550.59136	-0.03	0.03
60550.51038	0.06	0.03	60550.55087	-0.20	0.02	60550.59217	-0.08	0.03
60550.51119	0.05	0.03	60550.55168	-0.12	0.03	60550.59298	-0.04	0.03
60550.51200	0.04	0.03	60550.55249	-0.21	0.02	60550.59379	-0.00	0.03
60550.51281	0.01	0.03	60550.55330	-0.16	0.02	60550.59459	-0.04	0.03
60550.51362	0.06	0.03	60550.55411	-0.20	0.02	60550.59540	-0.04	0.03
60550.51443	0.13	0.03	60550.55492	-0.19	0.02	60550.59621	-0.01	0.03
60550.51524	0.29	0.04	60550.55573	-0.20	0.02	60550.59702	-0.06	0.03
60550.51605	0.41	0.04	60550.55654	-0.24	0.02	60550.59783	0.00	0.03
60550.51686	0.63	0.05	60550.55735	-0.29	0.02	60550.59864	-0.03	0.03
60550.51767	0.63	0.05	60550.55816	-0.23	0.02	60550.59945	0.00	0.03
60550.51848	0.68	0.05	60550.55897	-0.23	0.02	60550.60026	0.01	0.03
60550.51929	0.60	0.05	60550.55978	-0.20	0.02	60550.60107	0.06	0.03
60550.52010	0.50	0.04	60550.56059	-0.20	0.02	60550.60188	-0.04	0.03
60550.52091	0.46	0.04	60550.56140	-0.17	0.02	60550.60269	0.01	0.03
60550.52173	0.31	0.04	60550.56221	-0.16	0.02	60550.60350	0.03	0.03
60550.52254	0.22	0.03	60550.56302	-0.07	0.03	60550.60431	-0.06	0.03
60550.52335	0.13	0.03	60550.56382	-0.13	0.02	60550.60512	-0.04	0.03
60550.52416	0.07	0.03	60550.56463	-0.07	0.03	60550.60593	0.01	0.03
60550.52497	0.02	0.03	60550.56544	-0.11	0.03	60550.60674	0.11	0.03
60550.52578	0.02	0.03	60550.56625	-0.06	0.03	60550.60755	0.16	0.03
60550.52659	0.03	0.03	60550.56706	-0.12	0.03	60550.60836	0.27	0.04
60550.52739	-0.00	0.03	60550.56787	-0.12	0.03	60550.60916	0.41	0.04
60550.52820	0.02	0.03	60550.56868	-0.19	0.02	60550.60997	0.34	0.04
60550.52901	-0.03	0.03	60550.56949	-0.15	0.02	60550.61159	0.66	0.05
60550.52982	0.06	0.03	60550.57031	-0.21	0.02	60550.61240	0.55	0.05
60550.53063	0.04	0.03	60550.57112	-0.17	0.02	60550.61321	0.49	0.05
60550.53144	-0.05	0.03	60550.57193	-0.26	0.02	60550.61402	0.48	0.05
60550.53225	-0.01	0.03	60550.57274	-0.21	0.02	60550.61483	0.48	0.05
60550.53306	-0.03	0.03	60550.57355	-0.23	0.02	60550.61564	0.27	0.04
60550.53387	-0.07	0.03	60550.57436	-0.18	0.02	60550.61645	0.17	0.04

continued on the next page

Table 5 – continued from the previous page

HJD 2400000+ [d]	Mag [mag]	Err [mag]	HJD 2400000+ [d]	Mag [mag]	Err [mag]	HJD 2400000+ [d]	Mag [mag]	Err [mag]
60550.53468	0.00	0.03	60550.57517	-0.17	0.02	60550.61726	0.10	0.03
60550.53549	-0.08	0.03	60550.57598	-0.19	0.02	60550.61807	0.08	0.03
60550.53630	-0.06	0.03	60550.57679	-0.15	0.02	60550.61889	0.02	0.03
60550.53711	-0.01	0.03	60550.57760	-0.17	0.02	60550.61970	0.02	0.04
60550.53792	-0.06	0.03	60550.57841	-0.19	0.02	60550.62051	-0.00	0.04
60550.53873	-0.07	0.03	60550.57921	-0.18	0.02	60550.62132	0.00	0.04
60550.53954	-0.04	0.03	60550.58002	-0.15	0.02	60550.62213	-0.01	0.04
60550.54035	-0.09	0.03	60550.58083	-0.11	0.02	60550.62294	0.00	0.04
60550.54116	-0.10	0.03	60550.58164	-0.17	0.02			

Table 6: Photometric data for J296.1785+54.8285 in filter g'.

HJD 2400000+ [d]	Mag [mag]	Err [mag]	HJD 2400000+ [d]	Mag [mag]	Err [mag]	HJD 2400000+ [d]	Mag [mag]	Err [mag]
60550.34769	-0.21	0.01	60550.38941	-0.01	0.01	60550.43112	-0.01	0.01
60550.34804	-0.08	0.01	60550.38975	0.01	0.01	60550.43147	-0.04	0.01
60550.34839	-0.11	0.01	60550.39010	-0.00	0.01	60550.43181	-0.04	0.01
60550.34874	-0.13	0.01	60550.39045	-0.02	0.01	60550.43216	-0.03	0.01
60550.34908	-0.08	0.01	60550.39080	-0.03	0.01	60550.43251	-0.04	0.01
60550.34943	-0.07	0.01	60550.39114	-0.03	0.01	60550.43286	-0.02	0.01
60550.34978	0.15	0.01	60550.39149	-0.04	0.01	60550.43320	-0.04	0.01
60550.35013	0.03	0.01	60550.39184	-0.05	0.01	60550.43355	-0.03	0.01
60550.35048	-0.06	0.01	60550.39219	-0.04	0.01	60550.43391	-0.05	0.01
60550.35083	0.18	0.01	60550.39254	-0.05	0.01	60550.43426	-0.03	0.01
60550.35118	0.02	0.01	60550.39289	-0.05	0.01	60550.43460	-0.05	0.01
60550.35153	0.31	0.01	60550.39324	-0.07	0.01	60550.43495	-0.03	0.01
60550.35187	0.06	0.01	60550.39359	-0.07	0.01	60550.43530	-0.03	0.01
60550.35222	0.13	0.01	60550.39393	-0.07	0.01	60550.43565	-0.03	0.01
60550.35257	0.23	0.01	60550.39428	-0.06	0.01	60550.43599	-0.03	0.01
60550.35291	0.36	0.01	60550.39463	-0.05	0.01	60550.43634	-0.06	0.01
60550.35326	0.29	0.01	60550.39497	-0.05	0.01	60550.43669	-0.05	0.01
60550.35361	0.17	0.01	60550.39532	-0.06	0.01	60550.43703	-0.03	0.01
60550.35396	0.28	0.01	60550.39567	-0.05	0.01	60550.43738	-0.05	0.01
60550.35430	0.17	0.01	60550.39602	-0.05	0.01	60550.43773	-0.07	0.01
60550.35465	0.12	0.01	60550.39636	-0.04	0.01	60550.43808	-0.05	0.01
60550.35500	0.24	0.01	60550.39671	-0.04	0.01	60550.43842	-0.05	0.01
60550.35534	0.25	0.01	60550.39706	-0.05	0.01	60550.43877	-0.06	0.01
60550.35569	0.17	0.01	60550.39741	-0.05	0.01	60550.43912	-0.06	0.01
60550.35604	0.24	0.01	60550.39775	-0.05	0.01	60550.43947	-0.05	0.01
60550.35639	0.22	0.01	60550.39810	-0.04	0.01	60550.43981	-0.03	0.01
60550.35673	0.19	0.01	60550.39845	-0.02	0.01	60550.44016	-0.05	0.01
60550.35708	0.17	0.01	60550.39879	-0.05	0.01	60550.44051	-0.05	0.01
60550.35743	0.16	0.01	60550.39914	-0.05	0.01	60550.44085	-0.05	0.01
60550.35778	0.14	0.01	60550.39949	-0.05	0.01	60550.44120	-0.06	0.01
60550.35812	0.13	0.01	60550.39984	-0.06	0.01	60550.44155	-0.06	0.01
60550.35847	0.11	0.01	60550.40018	-0.04	0.01	60550.44190	-0.07	0.01
60550.35882	0.06	0.01	60550.40053	-0.04	0.01	60550.44224	-0.04	0.01
60550.35916	0.07	0.01	60550.40088	-0.03	0.01	60550.44259	-0.06	0.01
60550.35951	0.03	0.01	60550.40122	-0.04	0.01	60550.44294	-0.07	0.01
60550.35987	0.01	0.01	60550.40157	-0.03	0.01	60550.44328	-0.05	0.01
60550.36022	0.03	0.01	60550.40192	-0.03	0.01	60550.44363	-0.04	0.01
60550.36056	-0.03	0.01	60550.40228	-0.04	0.01	60550.44399	-0.06	0.01
60550.36091	-0.02	0.01	60550.40262	-0.02	0.01	60550.44434	-0.06	0.01
60550.36126	-0.03	0.01	60550.40297	-0.04	0.01	60550.44468	-0.05	0.01
60550.36161	-0.01	0.01	60550.40332	-0.04	0.01	60550.44503	-0.06	0.01
60550.36195	-0.02	0.01	60550.40367	-0.05	0.01	60550.44538	-0.06	0.01
60550.36230	-0.02	0.01	60550.40401	-0.03	0.01	60550.44573	-0.06	0.01
60550.36265	0.01	0.01	60550.40436	-0.04	0.01	60550.44607	-0.06	0.01
60550.36300	0.01	0.01	60550.40471	-0.05	0.01	60550.44642	-0.03	0.01
60550.36334	-0.03	0.01	60550.40506	-0.01	0.01	60550.44677	0.01	0.01
60550.36369	-0.03	0.01	60550.40540	-0.02	0.01	60550.44712	-0.03	0.01
60550.36404	-0.03	0.01	60550.40575	-0.03	0.01	60550.44746	-0.03	0.01
60550.36438	-0.01	0.01	60550.40610	-0.02	0.01	60550.44781	-0.02	0.01
60550.36473	-0.03	0.01	60550.40644	-0.01	0.01	60550.44816	-0.02	0.01
60550.36508	-0.03	0.01	60550.40679	-0.00	0.01	60550.44850	0.01	0.01
60550.36543	-0.02	0.01	60550.40714	0.00	0.01	60550.44885	-0.00	0.01

continued on the next page

Table 6 – continued from the previous page

HJD 2400000+ [d]	Mag [mag]	Err [mag]	HJD 2400000+ [d]	Mag [mag]	Err [mag]	HJD 2400000+ [d]	Mag [mag]	Err [mag]
60550.36577	-0.03	0.01	60550.40749	-0.01	0.01	60550.44920	0.01	0.01
60550.36612	-0.01	0.01	60550.40783	-0.02	0.01	60550.44955	0.03	0.01
60550.36647	-0.02	0.01	60550.40818	-0.02	0.01	60550.44989	0.01	0.01
60550.36681	-0.06	0.01	60550.40853	-0.01	0.01	60550.45024	0.04	0.01
60550.36716	-0.05	0.01	60550.40887	-0.01	0.01	60550.45059	-0.01	0.01
60550.36751	-0.02	0.01	60550.40922	0.00	0.01	60550.45093	0.03	0.01
60550.36786	-0.03	0.01	60550.40957	0.01	0.01	60550.45128	-0.01	0.01
60550.36820	-0.03	0.01	60550.40992	0.02	0.01	60550.45163	0.01	0.01
60550.36855	-0.04	0.01	60550.41026	-0.01	0.01	60550.45198	0.03	0.01
60550.36890	-0.04	0.01	60550.41061	-0.03	0.01	60550.45232	0.02	0.01
60550.36925	-0.06	0.01	60550.41096	-0.03	0.01	60550.45267	-0.02	0.01
60550.36959	-0.02	0.01	60550.41131	0.02	0.01	60550.45302	-0.00	0.01
60550.36994	-0.03	0.01	60550.41165	-0.01	0.01	60550.45337	0.02	0.01
60550.37029	-0.05	0.01	60550.41200	-0.02	0.01	60550.45371	-0.01	0.01
60550.37063	-0.03	0.01	60550.41235	0.01	0.01	60550.45406	0.03	0.01
60550.37099	-0.06	0.01	60550.41269	-0.00	0.01	60550.45441	-0.01	0.01
60550.37134	-0.05	0.01	60550.41304	0.02	0.01	60550.45475	-0.02	0.01
60550.37169	-0.04	0.01	60550.41339	0.02	0.01	60550.45510	-0.04	0.01
60550.37203	-0.03	0.01	60550.41374	0.02	0.01	60550.45546	-0.02	0.01
60550.37238	-0.06	0.01	60550.41408	0.01	0.01	60550.45581	-0.03	0.01
60550.37273	-0.04	0.01	60550.41443	0.01	0.01	60550.45615	-0.06	0.01
60550.37308	-0.06	0.01	60550.41478	0.04	0.01	60550.45650	-0.07	0.01
60550.37342	-0.05	0.01	60550.41512	0.10	0.01	60550.45685	-0.08	0.01
60550.37377	-0.07	0.01	60550.41547	0.09	0.01	60550.45720	0.02	0.01
60550.37412	-0.05	0.01	60550.41583	0.11	0.01	60550.45754	-0.07	0.01
60550.37447	-0.06	0.01	60550.41618	0.14	0.01	60550.45789	-0.07	0.01
60550.37481	-0.05	0.01	60550.41653	0.19	0.01	60550.45824	-0.06	0.01
60550.37516	-0.04	0.01	60550.41687	0.22	0.01	60550.45859	-0.04	0.01
60550.37551	-0.04	0.01	60550.41722	0.21	0.01	60550.45893	-0.06	0.01
60550.37585	-0.05	0.01	60550.41757	0.20	0.01	60550.45928	0.01	0.01
60550.37620	-0.04	0.01	60550.41791	0.19	0.01	60550.45963	-0.07	0.01
60550.37655	-0.05	0.01	60550.41826	0.20	0.01	60550.45997	-0.06	0.01
60550.37690	-0.06	0.01	60550.41861	0.20	0.01	60550.46032	-0.06	0.01
60550.37724	-0.05	0.01	60550.41896	0.19	0.01	60550.46067	-0.06	0.01
60550.37759	-0.06	0.01	60550.41930	0.21	0.01	60550.46102	-0.09	0.01
60550.37794	-0.06	0.01	60550.41965	0.20	0.01	60550.46136	-0.04	0.01
60550.37828	-0.06	0.01	60550.42000	0.20	0.01	60550.46171	-0.15	0.01
60550.37863	-0.05	0.01	60550.42034	0.26	0.01	60550.46206	-0.10	0.01
60550.37898	-0.05	0.01	60550.42069	0.22	0.01	60550.46240	-0.03	0.01
60550.37933	-0.06	0.01	60550.42104	0.21	0.01	60550.46275	-0.04	0.01
60550.37967	-0.07	0.01	60550.42139	0.18	0.01	60550.46311	0.06	0.01
60550.38002	-0.06	0.01	60550.42173	0.14	0.01	60550.46346	0.04	0.01
60550.38037	-0.07	0.01	60550.42208	0.14	0.01	60550.46381	-0.05	0.01
60550.38073	-0.07	0.01	60550.42243	0.12	0.01	60550.46415	-0.05	0.01
60550.38107	-0.07	0.01	60550.42278	0.11	0.01	60550.46450	-0.09	0.01
60550.38142	-0.07	0.01	60550.42312	0.07	0.01	60550.46485	-0.03	0.01
60550.38177	-0.04	0.01	60550.42347	0.03	0.01	60550.46519	-0.03	0.01
60550.38212	-0.06	0.01	60550.42382	-0.00	0.01	60550.46554	-0.15	0.01
60550.38246	-0.04	0.01	60550.42416	0.01	0.01	60550.46589	0.10	0.01
60550.38281	-0.02	0.01	60550.42451	-0.02	0.01	60550.46624	-0.06	0.01
60550.38316	-0.02	0.01	60550.42487	-0.01	0.01	60550.46658	0.05	0.01
60550.38350	0.01	0.01	60550.42522	-0.02	0.01	60550.46693	0.14	0.01
60550.38385	0.01	0.01	60550.42556	-0.01	0.01	60550.46728	-0.06	0.01
60550.38420	-0.01	0.01	60550.42591	-0.03	0.01	60550.46762	-0.05	0.01
60550.38455	-0.01	0.01	60550.42626	-0.01	0.01	60550.46797	0.07	0.01
60550.38489	-0.01	0.01	60550.42661	-0.01	0.01	60550.46832	0.10	0.01
60550.38524	0.02	0.01	60550.42695	-0.01	0.01	60550.46867	-0.05	0.01
60550.38559	0.00	0.01	60550.42730	-0.02	0.01	60550.46901	0.10	0.01
60550.38594	0.01	0.01	60550.42765	-0.03	0.01	60550.46936	-0.07	0.01
60550.38628	0.03	0.01	60550.42800	-0.00	0.01	60550.46971	0.05	0.01
60550.38663	0.01	0.01	60550.42834	-0.00	0.01	60550.47006	-0.08	0.01
60550.38698	0.02	0.01	60550.42869	-0.02	0.01	60550.47040	0.00	0.01
60550.38732	0.01	0.01	60550.42904	0.00	0.01	60550.47075	-0.06	0.01
60550.38767	0.01	0.01	60550.42938	0.00	0.01	60550.47110	-0.02	0.01
60550.38802	-0.02	0.01	60550.42973	-0.02	0.01	60550.47144	-0.14	0.01
60550.38837	-0.00	0.01	60550.43008	0.00	0.01	60550.47179	0.11	0.01
60550.38871	-0.00	0.01	60550.43043	-0.02	0.01	60550.47214	0.02	0.01
60550.38906	0.01	0.01	60550.43077	-0.03	0.01	60550.47249	0.13	0.01

Table 7: Photometric data for J296.1785+54.8285 in filter i'.

HJD 2400000+ [d]	Mag [mag]	Err [mag]	HJD 2400000+ [d]	Mag [mag]	Err [mag]	HJD 2400000+ [d]	Mag [mag]	Err [mag]
60552.55357	-0.07	0.01	60552.57818	-0.06	0.01	60552.60009	0.23	0.02
60552.55665	-0.06	0.01	60552.57854	-0.05	0.01	60552.60045	0.28	0.02
60552.55700	-0.08	0.01	60552.57890	-0.05	0.01	60552.60081	0.20	0.02
60552.55736	-0.08	0.01	60552.57926	-0.06	0.01	60552.60117	0.23	0.02
60552.55772	-0.08	0.01	60552.57962	-0.04	0.01	60552.60153	0.27	0.02
60552.55808	-0.08	0.01	60552.57998	-0.09	0.01	60552.60189	0.23	0.02
60552.55844	-0.07	0.01	60552.58034	-0.04	0.01	60552.60225	0.21	0.02
60552.55880	-0.06	0.01	60552.58070	-0.07	0.01	60552.60261	0.24	0.02
60552.55916	-0.08	0.01	60552.58105	-0.04	0.01	60552.60296	0.21	0.02
60552.55952	-0.07	0.01	60552.58141	-0.04	0.01	60552.60332	0.16	0.02
60552.55987	-0.09	0.01	60552.58177	-0.05	0.01	60552.60368	0.16	0.02
60552.56023	-0.09	0.01	60552.58213	-0.02	0.01	60552.60404	0.15	0.02
60552.56059	-0.08	0.01	60552.58250	-0.04	0.01	60552.60440	0.11	0.02
60552.56095	-0.07	0.01	60552.58286	-0.05	0.01	60552.60476	0.06	0.02
60552.56131	-0.07	0.01	60552.58322	-0.03	0.01	60552.60512	0.06	0.02
60552.56167	-0.10	0.01	60552.58358	-0.06	0.01	60552.60549	0.04	0.02
60552.56203	-0.08	0.01	60552.58394	-0.02	0.01	60552.60585	0.05	0.02
60552.56239	-0.08	0.01	60552.58430	-0.05	0.01	60552.60621	-0.02	0.02
60552.56274	-0.07	0.01	60552.58465	-0.02	0.01	60552.60656	0.01	0.02
60552.56310	-0.07	0.01	60552.58501	-0.03	0.01	60552.60692	0.03	0.02
60552.56346	-0.07	0.01	60552.58537	-0.03	0.01	60552.60728	0.01	0.02
60552.56382	-0.05	0.01	60552.58573	-0.03	0.01	60552.60764	0.01	0.02
60552.56418	-0.03	0.01	60552.58609	-0.02	0.01	60552.60800	0.02	0.02
60552.56454	-0.03	0.01	60552.58645	-0.02	0.01	60552.60872	0.02	0.02
60552.56490	-0.06	0.01	60552.58681	-0.06	0.01	60552.60908	0.00	0.02
60552.56526	-0.03	0.01	60552.58717	0.00	0.01	60552.60943	0.02	0.02
60552.56561	-0.02	0.01	60552.58752	-0.02	0.01	60552.60979	0.02	0.02
60552.56599	0.00	0.01	60552.58788	-0.02	0.01	60552.61015	-0.02	0.02
60552.56634	-0.01	0.01	60552.58824	-0.03	0.01	60552.61051	-0.00	0.02
60552.56670	0.03	0.01	60552.58860	-0.05	0.01	60552.61087	-0.05	0.02
60552.56706	0.01	0.01	60552.58896	0.00	0.01	60552.61123	-0.01	0.02
60552.56742	0.01	0.01	60552.58932	0.00	0.01	60552.61159	0.00	0.02
60552.56778	0.00	0.01	60552.58968	-0.02	0.01	60552.61195	-0.02	0.02
60552.56814	0.01	0.01	60552.59004	-0.03	0.01	60552.61230	-0.04	0.02
60552.56850	0.03	0.01	60552.59039	-0.00	0.01	60552.61266	-0.02	0.02
60552.56886	0.01	0.01	60552.59075	-0.03	0.01	60552.61302	-0.02	0.02
60552.56921	0.00	0.01	60552.59111	0.01	0.01	60552.61338	-0.02	0.02
60552.56957	-0.00	0.01	60552.59147	-0.04	0.01	60552.61374	-0.03	0.02
60552.56993	0.01	0.01	60552.59183	0.02	0.01	60552.61410	-0.02	0.02
60552.57029	0.01	0.01	60552.59219	-0.00	0.01	60552.61446	-0.01	0.02
60552.57065	0.00	0.01	60552.59255	-0.01	0.01	60552.61482	-0.03	0.02
60552.57101	-0.03	0.01	60552.59327	0.03	0.01	60552.61519	-0.04	0.02
60552.57137	-0.00	0.01	60552.59362	0.04	0.01	60552.61555	-0.05	0.02
60552.57173	-0.02	0.01	60552.59398	0.02	0.01	60552.61590	-0.06	0.02
60552.57244	-0.02	0.01	60552.59435	-0.01	0.01	60552.61626	-0.03	0.02
60552.57280	-0.03	0.01	60552.59471	0.01	0.01	60552.61662	0.03	0.02
60552.57316	-0.04	0.01	60552.59507	-0.02	0.01	60552.61698	-0.03	0.02
60552.57352	-0.05	0.01	60552.59543	0.01	0.02	60552.61734	-0.04	0.02
60552.57388	-0.08	0.01	60552.59579	0.05	0.02	60552.61770	-0.07	0.02
60552.57424	-0.05	0.01	60552.59615	0.05	0.02	60552.61806	-0.06	0.02
60552.57460	-0.07	0.01	60552.59651	0.09	0.02	60552.61842	-0.04	0.02
60552.57496	-0.05	0.01	60552.59686	0.14	0.02	60552.61877	-0.04	0.02
60552.57531	-0.08	0.01	60552.59722	0.12	0.02	60552.61913	-0.04	0.02
60552.57567	-0.08	0.01	60552.59758	0.13	0.02	60552.61949	-0.03	0.02
60552.57603	-0.09	0.01	60552.59794	0.19	0.02	60552.61985	-0.05	0.02
60552.57639	-0.08	0.01	60552.59830	0.20	0.02	60552.62021	-0.06	0.02
60552.57675	-0.06	0.01	60552.59866	0.21	0.02	60552.62057	-0.08	0.02
60552.57711	-0.06	0.01	60552.59902	0.24	0.02	60552.62093	0.07	0.02
60552.57747	-0.04	0.01	60552.59938	0.24	0.02			
60552.57783	-0.06	0.01	60552.59974	0.22	0.02			

Table 8: Photometric data for J296.1785+54.8285 in filter r'.

HJD 2400000+ [d]	Mag [mag]	Err [mag]	HJD 2400000+ [d]	Mag [mag]	Err [mag]	HJD 2400000+ [d]	Mag [mag]	Err [mag]
60554.28432	0.00	0.04	60554.32541	-0.04	0.01	60554.36275	-0.01	0.02
60554.28526	-0.05	0.03	60554.32577	-0.00	0.02	60554.36311	0.01	0.02
60554.28658	-0.04	0.03	60554.32613	-0.04	0.01	60554.36347	0.01	0.01
60554.28815	-0.08	0.03	60554.32649	0.02	0.02	60554.36382	0.00	0.01
60554.28950	-0.07	0.02	60554.32685	-0.02	0.01	60554.36418	-0.00	0.02
60554.28985	-0.10	0.02	60554.32720	0.00	0.01	60554.36454	-0.01	0.01
60554.29021	-0.04	0.02	60554.32756	-0.01	0.02	60554.36490	-0.00	0.02
60554.29057	-0.01	0.02	60554.32792	0.01	0.02	60554.36526	0.01	0.02
60554.29093	-0.10	0.02	60554.32828	0.03	0.02	60554.36562	0.02	0.02
60554.29129	-0.07	0.02	60554.32864	0.07	0.02	60554.36598	0.03	0.02
60554.29165	-0.12	0.02	60554.32900	0.05	0.02	60554.36634	0.01	0.02
60554.29201	-0.09	0.02	60554.32936	0.11	0.02	60554.36671	-0.01	0.01
60554.29237	-0.05	0.02	60554.32972	0.13	0.02	60554.36707	0.01	0.02
60554.29273	-0.03	0.02	60554.33007	0.20	0.02	60554.36742	0.03	0.02
60554.29308	-0.07	0.02	60554.33043	0.22	0.02	60554.36778	0.05	0.02
60554.29344	-0.05	0.02	60554.33079	0.21	0.02	60554.36814	0.01	0.02
60554.29380	-0.08	0.02	60554.33115	0.25	0.02	60554.36850	0.03	0.02
60554.29416	-0.07	0.02	60554.33151	0.26	0.02	60554.36886	0.00	0.02
60554.29452	-0.07	0.02	60554.33187	0.25	0.02	60554.36922	-0.03	0.01
60554.29488	-0.11	0.02	60554.33223	0.24	0.02	60554.36958	-0.06	0.01
60554.29524	-0.10	0.02	60554.33259	0.27	0.02	60554.36994	-0.07	0.01
60554.29560	-0.09	0.02	60554.33295	0.24	0.02	60554.37029	-0.02	0.01
60554.29595	-0.04	0.02	60554.33330	0.22	0.02	60554.37065	-0.08	0.01
60554.29631	-0.05	0.02	60554.33366	0.23	0.02	60554.37101	-0.07	0.01
60554.29667	-0.07	0.02	60554.33402	0.24	0.02	60554.37137	-0.08	0.01
60554.29703	-0.05	0.02	60554.33438	0.24	0.02	60554.37173	-0.06	0.01
60554.29739	-0.08	0.02	60554.33474	0.25	0.02	60554.37209	-0.07	0.01
60554.29775	-0.02	0.02	60554.33510	0.20	0.02	60554.37245	-0.05	0.01
60554.29811	0.00	0.02	60554.33546	0.19	0.02	60554.37281	-0.06	0.01
60554.29848	-0.00	0.02	60554.33582	0.19	0.02	60554.37316	-0.05	0.01
60554.29884	-0.03	0.02	60554.33617	0.13	0.02	60554.37352	-0.05	0.01
60554.29920	-0.03	0.02	60554.33653	0.11	0.02	60554.37388	-0.06	0.01
60554.29955	-0.02	0.02	60554.33689	0.05	0.02	60554.37425	-0.05	0.01
60554.29991	-0.03	0.02	60554.33725	0.09	0.02	60554.37461	-0.06	0.01
60554.30027	-0.01	0.02	60554.33761	0.04	0.02	60554.37497	-0.07	0.01
60554.30063	-0.02	0.02	60554.33797	-0.01	0.01	60554.37533	-0.07	0.01
60554.30099	-0.03	0.02	60554.33833	0.01	0.02	60554.37569	-0.03	0.01
60554.30135	-0.04	0.02	60554.33869	-0.02	0.01	60554.37605	-0.03	0.01
60554.30171	0.01	0.02	60554.33904	-0.02	0.01	60554.37641	-0.04	0.01
60554.30207	-0.03	0.02	60554.33940	-0.00	0.02	60554.37676	-0.04	0.01
60554.30242	-0.06	0.02	60554.33976	0.01	0.01	60554.37712	-0.05	0.01
60554.30278	-0.03	0.02	60554.34012	0.02	0.02	60554.37748	-0.01	0.02
60554.30314	-0.01	0.02	60554.34048	-0.02	0.01	60554.37784	-0.08	0.01
60554.30350	-0.02	0.02	60554.34085	0.01	0.01	60554.37820	-0.05	0.01
60554.30386	-0.03	0.02	60554.34121	-0.02	0.01	60554.37856	-0.05	0.01
60554.30422	-0.05	0.02	60554.34157	-0.00	0.02	60554.37892	-0.04	0.01
60554.30458	-0.01	0.02	60554.34193	-0.01	0.01	60554.37928	-0.02	0.02
60554.30494	-0.07	0.02	60554.34229	0.01	0.02	60554.37963	-0.05	0.01
60554.30529	-0.05	0.01	60554.34264	-0.01	0.01	60554.37999	-0.06	0.01
60554.30565	-0.06	0.01	60554.34300	-0.01	0.01	60554.38035	-0.04	0.02
60554.30601	-0.07	0.01	60554.34336	-0.01	0.01	60554.38071	-0.00	0.02
60554.30637	-0.10	0.01	60554.34372	-0.01	0.01	60554.38107	-0.05	0.01
60554.30673	-0.06	0.01	60554.34408	-0.01	0.01	60554.38143	-0.02	0.01
60554.30709	-0.07	0.01	60554.34444	0.00	0.01	60554.38179	-0.03	0.01
60554.30745	-0.06	0.01	60554.34480	-0.01	0.01	60554.38215	-0.03	0.01
60554.30781	-0.10	0.01	60554.34516	-0.03	0.01	60554.38250	-0.05	0.01
60554.30817	-0.08	0.01	60554.34551	-0.00	0.02	60554.38286	-0.01	0.02
60554.30852	-0.07	0.01	60554.34587	-0.03	0.01	60554.38322	-0.00	0.02
60554.30888	-0.05	0.01	60554.34623	-0.02	0.01	60554.38358	-0.03	0.02
60554.30924	-0.11	0.01	60554.34659	-0.03	0.01	60554.38395	0.00	0.02
60554.30960	-0.14	0.01	60554.34695	-0.03	0.01	60554.38431	-0.01	0.02
60554.30996	-0.06	0.01	60554.34731	-0.05	0.01	60554.38467	-0.01	0.02
60554.31032	-0.08	0.01	60554.34767	-0.04	0.01	60554.38503	-0.02	0.01
60554.31068	-0.06	0.01	60554.34803	-0.03	0.01	60554.38539	0.01	0.02
60554.31104	-0.06	0.01	60554.34838	-0.03	0.01	60554.38575	0.01	0.02
60554.31141	-0.06	0.01	60554.34874	-0.04	0.01	60554.38610	0.01	0.02

continued on the next page

Table 8 – continued from the previous page

HJD 2400000+ [d]	Mag [mag]	Err [mag]	HJD 2400000+ [d]	Mag [mag]	Err [mag]	HJD 2400000+ [d]	Mag [mag]	Err [mag]
60554.31176	-0.05	0.01	60554.34910	-0.02	0.01	60554.38646	-0.02	0.01
60554.31212	-0.06	0.01	60554.34946	-0.06	0.01	60554.38682	0.02	0.02
60554.31248	-0.08	0.01	60554.34982	-0.05	0.01	60554.38718	-0.01	0.01
60554.31284	-0.08	0.01	60554.35018	-0.03	0.01	60554.38754	-0.02	0.02
60554.31320	-0.05	0.01	60554.35054	-0.03	0.01	60554.38790	-0.01	0.02
60554.31356	-0.05	0.01	60554.35090	-0.07	0.01	60554.38826	-0.00	0.02
60554.31392	-0.06	0.01	60554.35126	-0.05	0.01	60554.38862	-0.01	0.01
60554.31428	-0.04	0.01	60554.35161	-0.02	0.01	60554.38897	0.01	0.02
60554.31463	-0.04	0.01	60554.35197	-0.06	0.01	60554.38933	0.01	0.02
60554.31499	-0.06	0.01	60554.35233	-0.07	0.01	60554.38969	-0.01	0.02
60554.31535	-0.08	0.01	60554.35269	-0.03	0.01	60554.39005	-0.00	0.02
60554.31571	-0.05	0.01	60554.35305	-0.05	0.01	60554.39041	0.01	0.02
60554.31607	-0.05	0.01	60554.35341	-0.04	0.01	60554.39077	0.04	0.02
60554.31643	-0.03	0.02	60554.35377	-0.05	0.01	60554.39113	0.01	0.02
60554.31679	-0.03	0.02	60554.35413	-0.05	0.01	60554.39149	0.02	0.02
60554.31715	-0.04	0.01	60554.35448	-0.03	0.01	60554.39185	-0.01	0.02
60554.31751	-0.02	0.01	60554.35485	-0.09	0.01	60554.39220	0.02	0.02
60554.31786	-0.00	0.02	60554.35521	-0.05	0.01	60554.39256	0.00	0.02
60554.31822	-0.03	0.01	60554.35557	-0.05	0.01	60554.39292	0.09	0.02
60554.31858	-0.05	0.01	60554.35593	-0.06	0.01	60554.39328	0.09	0.02
60554.31894	-0.03	0.02	60554.35629	-0.08	0.01	60554.39364	0.14	0.02
60554.31930	-0.04	0.01	60554.35665	-0.08	0.01	60554.39400	0.15	0.02
60554.31966	-0.06	0.01	60554.35701	-0.06	0.01	60554.39436	0.21	0.02
60554.32002	-0.02	0.01	60554.35737	-0.07	0.01	60554.39472	0.24	0.02
60554.32038	0.01	0.02	60554.35772	-0.05	0.01	60554.39507	0.24	0.02
60554.32073	-0.01	0.02	60554.35808	-0.08	0.01	60554.39543	0.25	0.02
60554.32109	-0.02	0.01	60554.35844	-0.07	0.01	60554.39579	0.24	0.02
60554.32145	-0.03	0.02	60554.35880	-0.07	0.01	60554.39615	0.26	0.02
60554.32181	-0.02	0.01	60554.35916	-0.07	0.01	60554.39652	0.27	0.02
60554.32217	-0.03	0.02	60554.35952	-0.06	0.01	60554.39688	0.28	0.02
60554.32253	-0.02	0.01	60554.35988	-0.05	0.01	60554.39724	0.24	0.02
60554.32289	-0.04	0.01	60554.36024	-0.04	0.01	60554.39760	0.22	0.02
60554.32325	-0.01	0.02	60554.36060	-0.05	0.01	60554.39796	0.29	0.02
60554.32360	-0.03	0.01	60554.36095	-0.05	0.01	60554.39832	0.22	0.02
60554.32396	-0.02	0.01	60554.36131	-0.04	0.02	60554.39867	0.24	0.02
60554.32432	-0.01	0.02	60554.36167	0.01	0.02	60554.39903	0.24	0.02
60554.32469	0.02	0.02	60554.36203	-0.00	0.01	60554.39939	0.20	0.02
60554.32505	-0.02	0.01	60554.36239	0.01	0.02	60554.39975	0.19	0.02

Table 9: Photometric data for J331.6658+32.7267 in filter i'.

HJD 2400000+ [d]	Mag [mag]	Err [mag]	HJD 2400000+ [d]	Mag [mag]	Err [mag]	HJD 2400000+ [d]	Mag [mag]	Err [mag]
60552.29532	0.10	0.03	60552.38254	-0.17	0.01	60552.45980	0.26	0.02
60552.29673	0.04	0.03	60552.38336	-0.16	0.01	60552.47541	0.20	0.02
60552.30456	0.01	0.02	60552.38418	-0.14	0.01	60552.47623	0.19	0.02
60552.30692	0.02	0.02	60552.38500	-0.14	0.01	60552.47705	0.19	0.02
60552.30775	0.01	0.02	60552.38583	-0.14	0.01	60552.47788	0.22	0.02
60552.30857	0.01	0.02	60552.38665	-0.13	0.01	60552.47870	0.21	0.02
60552.30939	-0.00	0.02	60552.38747	-0.14	0.01	60552.47952	0.19	0.02
60552.31021	-0.04	0.02	60552.38829	-0.13	0.01	60552.48034	0.12	0.03
60552.31103	-0.01	0.02	60552.38911	-0.10	0.01	60552.48116	0.24	0.06
60552.31186	-0.02	0.02	60552.38994	-0.12	0.01	60552.48199	0.36	0.08
60552.31268	-0.04	0.02	60552.39076	-0.12	0.01	60552.48281	0.32	0.06
60552.31350	-0.05	0.02	60552.39158	-0.10	0.01	60552.48363	0.14	0.03
60552.31432	-0.01	0.02	60552.39240	-0.10	0.01	60552.48445	0.24	0.03
60552.31514	-0.04	0.02	60552.39322	-0.07	0.01	60552.48527	0.21	0.02
60552.31596	-0.05	0.01	60552.39404	-0.11	0.01	60552.48609	0.23	0.02
60552.31679	-0.05	0.02	60552.39487	-0.10	0.01	60552.48692	0.20	0.02
60552.31761	-0.10	0.01	60552.39569	-0.07	0.01	60552.48774	0.20	0.02
60552.31843	-0.05	0.01	60552.39651	-0.05	0.01	60552.48856	0.18	0.02
60552.31925	-0.10	0.01	60552.39733	-0.10	0.01	60552.48938	0.19	0.02
60552.32007	-0.09	0.01	60552.39815	-0.07	0.01	60552.49020	0.15	0.02
60552.32090	-0.10	0.01	60552.39897	-0.04	0.01	60552.49102	0.18	0.02
60552.32172	-0.13	0.01	60552.39980	-0.06	0.01	60552.49185	0.18	0.02
60552.32254	-0.11	0.01	60552.40062	-0.08	0.01	60552.49267	0.17	0.02

continued on the next page

Table 9 – continued from the previous page

HJD 2400000+ [d]	Mag [mag]	Err [mag]	HJD 2400000+ [d]	Mag [mag]	Err [mag]	HJD 2400000+ [d]	Mag [mag]	Err [mag]
60552.32336	-0.12	0.01	60552.40144	-0.05	0.01	60552.49349	0.15	0.02
60552.32418	-0.13	0.01	60552.40226	-0.04	0.01	60552.49431	0.16	0.02
60552.32500	-0.14	0.01	60552.40308	-0.06	0.01	60552.49513	0.20	0.02
60552.32583	-0.13	0.01	60552.40391	-0.05	0.01	60552.49596	0.20	0.02
60552.32747	-0.16	0.01	60552.40473	-0.04	0.01	60552.49678	0.17	0.03
60552.32829	-0.16	0.01	60552.40555	-0.02	0.01	60552.49760	0.10	0.03
60552.32911	-0.15	0.01	60552.40637	-0.00	0.01	60552.49842	0.09	0.03
60552.32993	-0.19	0.01	60552.40719	-0.01	0.01	60552.49924	0.12	0.03
60552.33076	-0.18	0.01	60552.40801	0.00	0.01	60552.50006	0.14	0.03
60552.33159	-0.18	0.01	60552.40884	0.02	0.01	60552.50089	0.07	0.03
60552.33241	-0.18	0.01	60552.40966	0.01	0.01	60552.50171	0.17	0.08
60552.33323	-0.18	0.01	60552.41048	0.02	0.01	60552.50253	0.10	0.10
60552.33406	-0.19	0.01	60552.41130	0.00	0.01	60552.50335	0.40	0.10
60552.33488	-0.21	0.01	60552.41212	0.01	0.01	60552.50417	0.21	0.06
60552.33570	-0.22	0.01	60552.41295	0.02	0.01	60552.50498	0.22	0.05
60552.33652	-0.18	0.01	60552.41377	0.04	0.01	60552.50581	0.13	0.05
60552.33734	-0.21	0.01	60552.41459	0.05	0.01	60552.50663	0.13	0.04
60552.33816	-0.21	0.01	60552.41541	0.02	0.01	60552.50746	0.18	0.05
60552.33899	-0.22	0.01	60552.41623	0.05	0.01	60552.50828	0.18	0.06
60552.33981	-0.21	0.01	60552.41705	0.06	0.02	60552.50910	0.11	0.06
60552.34063	-0.21	0.01	60552.41788	0.04	0.01	60552.50991	0.19	0.05
60552.34145	-0.20	0.01	60552.41870	0.05	0.01	60552.51074	0.11	0.05
60552.34227	-0.21	0.01	60552.41952	0.04	0.01	60552.51156	0.03	0.05
60552.34309	-0.21	0.01	60552.42034	0.06	0.01	60552.51238	0.17	0.05
60552.34392	-0.20	0.01	60552.42116	0.07	0.01	60552.51320	0.16	0.04
60552.34474	-0.22	0.01	60552.42198	0.06	0.01	60552.51403	0.12	0.03
60552.34556	-0.19	0.01	60552.42281	0.07	0.02	60552.51486	0.09	0.03
60552.34638	-0.20	0.01	60552.42363	0.08	0.02	60552.51568	0.05	0.03
60552.34720	-0.21	0.01	60552.42446	0.05	0.01	60552.51649	0.13	0.03
60552.34803	-0.22	0.01	60552.42528	0.09	0.02	60552.51732	0.13	0.03
60552.34885	-0.18	0.01	60552.42610	0.07	0.02	60552.51814	0.00	0.03
60552.34967	-0.16	0.01	60552.42693	0.09	0.02	60552.51897	0.08	0.03
60552.35049	-0.15	0.01	60552.42775	0.11	0.02	60552.51979	0.11	0.02
60552.35131	-0.14	0.01	60552.42857	0.09	0.02	60552.52061	0.17	0.02
60552.35213	-0.12	0.01	60552.42939	0.09	0.02	60552.52143	0.09	0.02
60552.35296	-0.11	0.01	60552.43021	0.08	0.01	60552.52225	0.10	0.02
60552.35378	-0.11	0.01	60552.43104	0.10	0.02	60552.52307	-0.05	0.03
60552.35460	-0.11	0.01	60552.43186	0.09	0.01	60552.52390	-0.03	0.03
60552.35542	-0.10	0.01	60552.43268	0.09	0.01	60552.52472	0.05	0.03
60552.35624	-0.09	0.01	60552.43350	0.10	0.01	60552.52554	0.03	0.03
60552.35706	-0.14	0.01	60552.43432	0.09	0.02	60552.52636	-0.04	0.03
60552.35789	-0.13	0.01	60552.43514	0.11	0.01	60552.52718	0.02	0.03
60552.35871	-0.15	0.01	60552.43597	0.11	0.02	60552.52800	-0.04	0.03
60552.35953	-0.14	0.01	60552.43679	0.11	0.02	60552.52883	0.10	0.02
60552.36035	-0.17	0.01	60552.43761	0.13	0.02	60552.52965	0.08	0.02
60552.36117	-0.20	0.01	60552.43843	0.11	0.01	60552.53047	0.06	0.02
60552.36200	-0.19	0.01	60552.43925	0.12	0.02	60552.53129	0.02	0.02
60552.36282	-0.22	0.01	60552.44008	0.11	0.02	60552.53211	0.05	0.02
60552.36364	-0.23	0.01	60552.44090	0.12	0.02	60552.53294	0.05	0.02
60552.36446	-0.23	0.01	60552.44172	0.15	0.02	60552.53376	0.01	0.02
60552.36528	-0.21	0.01	60552.44254	0.11	0.02	60552.53458	0.02	0.02
60552.36610	-0.25	0.01	60552.44336	0.11	0.02	60552.53540	0.01	0.02
60552.36693	-0.23	0.01	60552.44418	0.11	0.02	60552.53622	-0.02	0.02
60552.36775	-0.21	0.01	60552.44501	0.13	0.02	60552.53704	0.00	0.02
60552.36857	-0.20	0.01	60552.44583	0.12	0.02	60552.53787	0.00	0.02
60552.36939	-0.20	0.01	60552.44665	0.14	0.02	60552.53869	-0.00	0.02
60552.37021	-0.22	0.01	60552.44747	0.14	0.02	60552.53951	-0.01	0.02
60552.37103	-0.21	0.01	60552.44829	0.12	0.02	60552.54033	0.01	0.02
60552.37186	-0.20	0.01	60552.44911	0.15	0.02	60552.54115	-0.01	0.02
60552.37268	-0.22	0.01	60552.44994	0.14	0.02	60552.54197	-0.01	0.02
60552.37350	-0.21	0.01	60552.45076	0.15	0.02	60552.54280	-0.03	0.02
60552.37432	-0.22	0.01	60552.45158	0.13	0.02	60552.54362	0.00	0.02
60552.37514	-0.22	0.01	60552.45240	0.15	0.02	60552.54444	-0.11	0.03
60552.37597	-0.20	0.01	60552.45322	0.17	0.02	60552.54526	-0.05	0.04
60552.37679	-0.20	0.01	60552.45405	0.13	0.02	60552.54608	-0.06	0.02
60552.37761	-0.19	0.01	60552.45487	0.19	0.02	60552.54691	-0.06	0.02
60552.37843	-0.20	0.01	60552.45569	0.24	0.02	60552.54773	-0.09	0.02
60552.37925	-0.19	0.01	60552.45651	0.33	0.02	60552.54855	-0.15	0.02

continued on the next page

Table 9 – continued from the previous page

HJD 2400000+ [d]	Mag [mag]	Err [mag]	HJD 2400000+ [d]	Mag [mag]	Err [mag]	HJD 2400000+ [d]	Mag [mag]	Err [mag]
60552.38007	-0.14	0.01	60552.45733	0.41	0.02	60552.55019	-0.10	0.03
60552.38090	-0.18	0.01	60552.45815	0.55	0.02			
60552.38172	-0.19	0.01	60552.45898	0.35	0.02			

Appendix D Data from the Mount Suhora Observatory

Table 10: Photometric data for J018.4128+22.9608 in filter *B*.

HJD 2400000+ [d]	Mag [mag]	Err [mag]	HJD 2400000+ [d]	Mag [mag]	Err [mag]	HJD 2400000+ [d]	Mag [mag]	Err [mag]
61059.23292	-0.02	0.02	61060.29288	-0.12	0.02	61061.29743	-0.06	0.02
61059.23995	-0.10	0.02	61060.29713	-0.16	0.02	61061.30168	-0.07	0.02
61059.24697	-0.10	0.02	61060.30138	-0.12	0.02	61061.30592	-0.11	0.02
61059.25503	-0.16	0.01	61060.30562	-0.08	0.02	61061.31017	-0.12	0.02
61059.26205	-0.05	0.02	61060.30987	-0.03	0.02	61061.31442	-0.05	0.02
61059.26908	-0.12	0.02	61060.31412	-0.04	0.02	61061.31867	-0.08	0.02
61059.27610	-0.06	0.02	61060.31837	-0.00	0.02	61061.32291	-0.14	0.02
61059.28312	-0.06	0.02	61060.32261	0.04	0.02	61061.32716	-0.07	0.02
61059.29716	-0.02	0.02	61060.32685	0.02	0.02	61061.33140	-0.08	0.02
61059.30419	0.16	0.02	61060.33110	0.14	0.02	61061.33565	-0.06	0.02
61059.31121	0.37	0.02	61060.33534	0.63	0.03	61061.34188	-0.03	0.02
61059.31824	0.01	0.02	61060.33959	0.20	0.02	61061.34613	-0.01	0.02
61059.32526	-0.03	0.02	61060.34384	0.03	0.02	61061.35038	0.02	0.02
61059.33229	-0.04	0.02	61060.34808	0.01	0.02	61061.35462	0.08	0.03
61059.33931	-0.08	0.02	61060.35233	0.02	0.02	61061.35887	0.18	0.03
61059.34633	-0.11	0.02	61060.35657	-0.05	0.02	61061.36311	0.61	0.04
61059.35336	-0.05	0.02	61060.36082	-0.08	0.02	61061.36736	0.17	0.03
61059.36038	-0.11	0.02	61061.21674	-0.14	0.02	61061.37160	0.06	0.03
61059.36740	-0.11	0.02	61061.22099	-0.07	0.02	61061.37585	0.03	0.03
61059.37443	-0.05	0.02	61061.22524	-0.10	0.02	61061.38009	-0.04	0.03
61059.38145	-0.00	0.02	61061.22948	-0.11	0.02	61062.19124	-0.02	0.02
61060.22493	-0.02	0.02	61061.23373	-0.15	0.02	61062.19549	-0.00	0.02
61060.23342	0.02	0.02	61061.23797	-0.11	0.02	61062.19974	0.24	0.02
61060.23767	0.12	0.02	61061.24222	-0.04	0.02	61062.20399	0.55	0.02
61060.24192	0.61	0.03	61061.24647	-0.04	0.02	61062.20824	0.02	0.02
61060.24616	0.18	0.02	61061.25071	-0.04	0.02	61062.21248	-0.04	0.01
61060.25041	-0.02	0.02	61061.25496	0.02	0.02	61062.21673	-0.05	0.02
61060.25465	-0.03	0.02	61061.25920	-0.00	0.02	61062.22098	-0.03	0.01
61060.25889	-0.02	0.02	61061.26346	0.04	0.02	61062.22947	-0.07	0.01
61060.26314	-0.07	0.02	61061.26770	0.49	0.03	61062.23372	-0.12	0.01
61060.26739	-0.09	0.02	61061.27195	0.34	0.03	61062.23797	-0.13	0.01
61060.27163	-0.11	0.02	61061.27619	0.02	0.02	61062.24221	-0.16	0.01
61060.27588	-0.13	0.02	61061.28044	-0.00	0.02	61062.24646	-0.12	0.01
61060.28012	-0.16	0.02	61061.28469	-0.03	0.02	61062.25071	-0.08	0.01
61060.28437	-0.10	0.02	61061.28893	-0.06	0.02			
61060.28862	-0.02	0.02	61061.29319	-0.02	0.02			

Table 11: Photometric data for J018.4128+22.9608 in filter *V*.

HJD 2400000+ [d]	Mag [mag]	Err [mag]	HJD 2400000+ [d]	Mag [mag]	Err [mag]	HJD 2400000+ [d]	Mag [mag]	Err [mag]
61059.22780	0.06	0.02	61060.28649	-0.12	0.02	61061.29956	-0.11	0.02
61059.23644	0.00	0.02	61060.29075	-0.12	0.02	61061.30380	-0.13	0.02
61059.24346	-0.07	0.02	61060.29500	-0.17	0.02	61061.30805	-0.09	0.02
61059.25049	-0.08	0.02	61060.29925	-0.16	0.02	61061.31229	-0.09	0.02
61059.25854	-0.09	0.02	61060.30350	-0.13	0.02	61061.31654	-0.04	0.02
61059.26557	-0.05	0.02	61060.30775	-0.10	0.02	61061.32079	-0.09	0.02
61059.27259	-0.10	0.02	61060.31199	-0.06	0.02	61061.32503	-0.12	0.02
61059.27961	-0.05	0.02	61060.31624	-0.03	0.02	61061.32928	-0.08	0.02
61059.28663	-0.01	0.02	61060.32049	0.02	0.03	61061.33353	-0.08	0.03

continued on the next page

Table 11 – continued from the previous page

HJD 2400000+ [d]	Mag [mag]	Err [mag]	HJD 2400000+ [d]	Mag [mag]	Err [mag]	HJD 2400000+ [d]	Mag [mag]	Err [mag]
61059.29365	0.05	0.02	61060.32473	-0.00	0.03	61061.33777	-0.04	0.03
61059.30068	0.07	0.02	61060.32898	-0.01	0.03	61061.34400	-0.05	0.03
61059.30770	0.62	0.04	61060.33322	0.42	0.04	61061.34825	0.07	0.03
61059.31472	-0.02	0.02	61060.33746	0.54	0.04	61061.35250	-0.04	0.03
61059.32175	-0.00	0.03	61060.34171	0.04	0.03	61061.35674	0.08	0.03
61059.32877	-0.09	0.02	61060.34596	0.04	0.03	61061.36099	0.62	0.05
61059.33580	-0.07	0.02	61060.35020	0.03	0.03	61061.36523	0.45	0.05
61059.34282	-0.08	0.02	61060.35445	-0.02	0.03	61061.36948	0.05	0.03
61059.34984	-0.10	0.02	61060.35869	-0.04	0.03	61061.37372	0.02	0.03
61059.35687	-0.09	0.02	61060.36294	-0.10	0.03	61061.37797	-0.04	0.03
61059.36389	-0.16	0.02	61061.21887	-0.17	0.02	61061.38221	0.09	0.03
61059.37092	-0.06	0.03	61061.22311	-0.08	0.02	61062.19337	-0.04	0.02
61059.37794	0.03	0.03	61061.22736	-0.15	0.02	61062.19762	0.05	0.02
61059.38496	0.01	0.03	61061.23161	-0.20	0.02	61062.20186	0.67	0.04
61060.22706	-0.10	0.02	61061.23585	-0.15	0.02	61062.20611	0.30	0.03
61060.23130	-0.03	0.02	61061.24010	-0.10	0.02	61062.21036	-0.02	0.02
61060.23555	0.00	0.02	61061.24435	-0.09	0.02	61062.21461	-0.00	0.02
61060.23979	0.40	0.03	61061.24859	-0.04	0.02	61062.21886	-0.01	0.02
61060.24404	0.50	0.03	61061.25283	-0.05	0.02	61062.22311	-0.06	0.02
61060.24828	0.06	0.02	61061.25708	-0.02	0.02	61062.22735	-0.03	0.02
61060.25253	-0.01	0.02	61061.26133	0.03	0.02	61062.23160	-0.06	0.02
61060.25677	-0.04	0.02	61061.26982	0.55	0.04	61062.23585	-0.06	0.02
61060.26102	-0.05	0.02	61061.27407	0.05	0.03	61062.24009	-0.16	0.02
61060.26527	-0.05	0.02	61061.27832	0.04	0.02	61062.24434	-0.19	0.02
61060.26951	-0.08	0.02	61061.28257	0.01	0.03	61062.24858	-0.03	0.02
61060.27375	-0.13	0.02	61061.28681	0.02	0.03	61062.25283	-0.06	0.02
61060.27800	-0.19	0.02	61061.29106	-0.07	0.02			
61060.28224	-0.18	0.02	61061.29531	-0.09	0.02			

Table 12: Photometric data for J296.1785+54.8285 in filter *B*.

HJD 2400000+ [d]	Mag [mag]	Err [mag]	HJD 2400000+ [d]	Mag [mag]	Err [mag]	HJD 2400000+ [d]	Mag [mag]	Err [mag]
61059.62560	-0.03	0.01	61105.55209	0.20	0.01	61109.52186	0.01	0.02
61059.63262	-0.05	0.01	61105.55633	-0.02	0.01	61109.52610	0.20	0.02
61059.63965	0.02	0.01	61105.56058	-0.02	0.01	61109.53035	0.19	0.02
61059.64667	-0.06	0.01	61105.56482	-0.08	0.01	61109.53460	0.00	0.02
61059.65369	-0.04	0.01	61105.56907	-0.06	0.01	61109.53884	-0.00	0.02
61059.66071	-0.01	0.01	61105.57332	-0.04	0.01	61109.54309	-0.06	0.01
61059.66774	-0.02	0.01	61105.57756	-0.05	0.01	61109.54733	-0.03	0.01
61059.67476	0.21	0.01	61105.58181	0.00	0.01	61109.55158	-0.05	0.01
61061.62849	-0.01	0.02	61105.58606	-0.04	0.01	61109.55583	0.00	0.01
61061.63274	0.01	0.02	61105.59031	-0.06	0.01	61109.56007	0.01	0.01
61061.63699	-0.06	0.02	61105.59455	-0.05	0.01	61109.56432	-0.02	0.01
61061.64123	-0.04	0.02	61105.59880	-0.07	0.01	61109.56857	-0.05	0.01
61061.64548	-0.03	0.02	61105.60305	-0.04	0.01	61109.57282	-0.07	0.01
61061.64972	-0.03	0.01	61105.60729	-0.02	0.01	61109.57706	-0.04	0.01
61061.65397	-0.02	0.01	61105.61154	0.18	0.01	61109.58131	-0.01	0.01
61061.65822	0.02	0.01	61105.61578	0.20	0.01	61109.58556	-0.01	0.01
61061.66246	0.23	0.01	61105.62003	-0.03	0.01	61109.58981	0.19	0.02
61061.66671	0.08	0.01	61105.62428	-0.04	0.01	61109.59406	0.21	0.01
61061.67522	-0.03	0.01	61105.62853	-0.04	0.01	61109.59830	0.01	0.01
61105.47988	-0.00	0.02	61105.63277	-0.07	0.01	61109.60255	-0.00	0.01
61105.48413	0.21	0.02	61105.63702	-0.06	0.01	61109.60679	-0.05	0.01
61105.48838	0.19	0.02	61105.64127	-0.07	0.01	61109.61104	-0.05	0.01
61105.49263	-0.02	0.01	61105.64551	-0.01	0.01	61109.61529	-0.07	0.01
61105.49687	-0.04	0.01	61105.65401	-0.09	0.01	61109.61954	-0.05	0.01
61105.50112	-0.00	0.01	61105.65826	-0.06	0.01	61109.62378	0.02	0.01
61105.50537	-0.09	0.01	61105.66250	-0.08	0.01	61109.62802	-0.03	0.01
61105.50961	-0.05	0.01	61105.66675	-0.04	0.01	61109.63227	-0.08	0.01
61105.51386	-0.05	0.02	61105.67099	0.00	0.02	61109.64076	-0.05	0.01
61105.51810	0.00	0.02	61105.67524	0.18	0.02	61109.64501	-0.02	0.01
61105.52235	-0.02	0.02	61109.49212	-0.00	0.01	61109.64925	-0.03	0.01
61105.52661	-0.06	0.02	61109.49637	0.01	0.01	61109.65350	0.13	0.02
61105.53086	-0.02	0.02	61109.50062	-0.03	0.01	61109.65775	0.16	0.02
61105.53510	-0.04	0.01	61109.50487	-0.06	0.01	61109.66200	0.01	0.02

continued on the next page

Table 12 – continued from the previous page

HJD 2400000+ [d]	Mag [mag]	Err [mag]	HJD 2400000+ [d]	Mag [mag]	Err [mag]	HJD 2400000+ [d]	Mag [mag]	Err [mag]
61105.53935	-0.03	0.01	61109.50912	-0.07	0.01	61109.66624	0.01	0.03
61105.54359	-0.00	0.01	61109.51336	-0.04	0.01	61109.67049	-0.08	0.05
61105.54784	0.18	0.01	61109.51761	-0.01	0.01			

Table 13: Photometric data for J296.1785+54.8285 in filter V.

HJD 2400000+ [d]	Mag [mag]	Err [mag]	HJD 2400000+ [d]	Mag [mag]	Err [mag]	HJD 2400000+ [d]	Mag [mag]	Err [mag]
61059.62911	0.01	0.01	61105.55421	0.07	0.01	61109.52398	0.05	0.01
61059.63613	-0.04	0.01	61105.55846	-0.03	0.01	61109.52823	0.21	0.02
61059.64316	0.02	0.01	61105.56270	-0.04	0.01	61109.53247	0.01	0.01
61059.65018	-0.04	0.01	61105.56695	-0.06	0.01	61109.53672	-0.03	0.01
61059.65720	-0.03	0.01	61105.57119	-0.08	0.01	61109.54097	-0.05	0.01
61059.66423	0.02	0.01	61105.57544	-0.09	0.01	61109.54521	-0.04	0.01
61059.67125	0.17	0.01	61105.57968	-0.01	0.01	61109.54946	-0.05	0.01
61059.67827	0.10	0.01	61105.58393	0.00	0.01	61109.55371	-0.06	0.01
61061.63062	-0.00	0.02	61105.58818	-0.04	0.01	61109.55795	0.01	0.01
61061.63486	-0.01	0.02	61105.59243	-0.05	0.01	61109.56219	-0.01	0.01
61061.63911	-0.04	0.02	61105.59667	-0.08	0.01	61109.56644	-0.09	0.01
61061.64336	0.01	0.02	61105.60092	-0.07	0.01	61109.57069	-0.06	0.01
61061.64760	-0.03	0.02	61105.60517	-0.02	0.01	61109.57494	-0.07	0.01
61061.65185	-0.01	0.01	61105.60942	0.02	0.01	61109.57919	-0.03	0.01
61061.65609	0.02	0.01	61105.61366	0.21	0.01	61109.58343	-0.03	0.01
61061.66034	0.23	0.02	61105.61791	0.11	0.01	61109.58768	0.04	0.01
61061.66459	0.22	0.02	61105.62215	-0.02	0.01	61109.59193	0.22	0.01
61061.66884	-0.00	0.01	61105.62640	-0.02	0.01	61109.59618	0.05	0.01
61061.67309	-0.02	0.01	61105.63065	-0.06	0.01	61109.60042	-0.06	0.01
61061.67734	-0.01	0.01	61105.63489	-0.07	0.01	61109.60467	-0.03	0.01
61105.48201	0.10	0.02	61105.63914	-0.07	0.01	61109.60892	-0.07	0.01
61105.48626	0.21	0.02	61105.64339	-0.01	0.01	61109.61317	-0.04	0.01
61105.49051	0.03	0.01	61105.64764	-0.02	0.01	61109.61741	-0.06	0.01
61105.49475	-0.02	0.01	61105.65189	-0.08	0.01	61109.62166	0.01	0.01
61105.49900	-0.04	0.01	61105.65613	-0.06	0.01	61109.62590	-0.01	0.01
61105.50324	-0.06	0.01	61105.66038	-0.05	0.01	61109.63015	-0.07	0.01
61105.50749	-0.07	0.01	61105.66463	-0.03	0.01	61109.63439	-0.05	0.01
61105.51174	-0.05	0.01	61105.66887	-0.01	0.01	61109.63864	-0.07	0.01
61105.51598	0.02	0.02	61105.67312	0.01	0.01	61109.64289	-0.02	0.01
61105.52023	0.03	0.02	61105.67736	0.21	0.02	61109.64713	-0.03	0.01
61105.52448	-0.06	0.02	61109.49425	-0.01	0.01	61109.65138	0.03	0.01
61105.52873	-0.05	0.01	61109.49850	0.00	0.01	61109.65563	0.20	0.01
61105.53298	-0.04	0.01	61109.50274	-0.05	0.01	61109.65987	0.10	0.01
61105.53723	-0.06	0.01	61109.50699	-0.04	0.01	61109.66412	0.00	0.02
61105.54147	-0.02	0.01	61109.51124	-0.05	0.01	61109.66837	-0.05	0.02
61105.54572	0.07	0.01	61109.51548	-0.04	0.01			
61105.54996	0.20	0.01	61109.51973	-0.03	0.01			

Bibliography

Allers, K. N., & Liu, M. C. (2013). A near-infrared spectroscopic study of young field ultracool dwarfs. *The Astrophysical Journal*, *772*(2), 79. https://doi.org/10.1088/0004-637x/772/2/79

Altunbulak, M., & Klyachko, A. (2008). The Pauli Principle Revisited. *Communications in Mathematical Physics*, *282*(2), 287–322. https://doi.org/10.1007/s00220-008-0552-z

André, P., Men'shchikov, A., Bontemps, S., Könyves, V., Motte, F., Schneider, N., Didelon, P., Minier, V., Saraceno, P., Ward-Thompson, D., di Francesco, J., White, G., Molinari, S., Testi, L., Abergel, A., Griffin, M., Henning, T., Royer, P., Merín, B., . . . Zavagno, A. (2010). From filamentary clouds to prestellar cores to the stellar IMF: Initial highlights from the Herschel Gould Belt Survey., *518*, Article L102, L102. https://doi.org/10.1051/0004-6361/201014666

Apellániz, J. M., Negueruela, I., & Caballero, J. A. (2024). Spectral classification. https://arxiv.org/abs/2410.07301

Arzoumanian, D., André, P., Didelon, P., Könyves, V., Schneider, N., Men'shchikov, A., Sousbie, T., Zavagno, A., Bontemps, S., Di Francesco, J., Griffin, M., Hennemann, M., Hill, T., Kirk, J., Martin, P., Minier, V., Molinari, S., Motte, F., Peretto, N., . . . Wilson, C. D. (2011). Characterizing interstellar filaments withherschelin ic 5146. *Astronomy amp; Astrophysics*, *529*, L6. https://doi.org/10.1051/0004-6361/201116596

Barnes, J. (1993). *A Beginner's Guide to Using IRAF*. https://iraf-community.github.io/doc/beguide.pdf

Bate, M. R., Bonnell, I. A., & Bromm, V. (2002). The formation mechanism of brown dwarfs. *Monthly Notices of the Royal Astronomical Society*, *332*(3), L65–L68. https://doi.org/10.1046/j.1365-8711.2002.05539.x

Béjar, V. J. S., Zapatero Osorio, M. R., & Rebolo, R. (1999). A Search for Very Low Mass Stars and Brown Dwarfs in the Young σ Orionis Cluster., *521*(2), 671–681. https://doi.org/10.1086/307583

Berry, R., & Burnell, J. (2005). *The handbook of astronomical image processing* (Vol. 2).

Bildsten, L., Brown, E. F., Matzner, C. D., & Ushomirsky, G. (1997). Lithium depletion in fully convective pre-main-sequence stars. *The Astrophysical Journal*, *482*(1), 442. https://doi.org/10.1086/304151

Bonnell, I. A., Bate, M. R., Clarke, C. J., & Pringle, J. E. (1997). Accretion and the stellar mass spectrum in small clusters. *Monthly Notices of the Royal Astronomical Society*, *285*(1), 201–208. https://doi.org/10.1093/mnras/285.1.201

Burrows, A., Hubbard, W. B., Lunine, J. I., & Liebert, J. (2001). The theory of brown dwarfs and extrasolar giant planets. *Reviews of Modern Physics*, *73*(3), 719–765. https://doi.org/10.1103/RevModPhys.73.719

Burrows, A., & Liebert, J. (1993). The science of brown dwarfs. *Reviews of Modern Physics*, *65*(2), 301–336. https://doi.org/10.1103/RevModPhys.65.301

Chabrier, G., & Baraffe, I. (2000). Theory of Low-Mass Stars and Substellar Objects., *38*, 337–377. https://doi.org/10.1146/annurev.astro.38.1.337

Cruz, K. L., Kirkpatrick, J. D., & Burgasser, A. J. (2009). Young l dwarfs identified in the field: A preliminary low-gravity, optical spectral sequence from l0 to l5. *The Astronomical Journal*, *137*(2), 3345–3357. https://doi.org/10.1088/0004-6256/137/2/3345

D'Antona, F., & Mazzitelli, I. (1994). New Pre–Main-Sequence Tracks for M $\leq$ 2.5 $M_{\odot}$ as Tests of Opacities and Convection Model., *90*, 467. https://doi.org/10.1086/191867

Dawson, H. (2024, August). Data reduction II, Photometry with IRAF. https://stel.asu.cas.cz/en/wp%20content/uploads/2024/08/Photometry˙reduction˙Harry˙v2.pdf

Gargaud, M., Irvine, W. M., Amils, R., Claeys, P., Cleaves, H. J., Gerin, M., Rouan, D., Spohn, T., Tirard, S., & Viso, M. (2023). *Encyclopedia of Astrobiology*. Springer-Verlag Berlin Heidelberg. https://doi.org/10.1007/978-3-662-65093-6

Gray, R. O., & Corbally, C., J. (2009). *Stellar Spectral Classification*. Princeton University Press.

Hayek, W., Sing, D., Pont, F., & Asplund, M. (2012). Limb darkening laws for two exoplanet host stars derived from 3D stellar model atmospheres: Comparison with 1D models and HST light curve observations. *Astronomy amp; Astrophysics*, *539*, A102. https://doi.org/10.1051/0004-6361/201117868

Hubber, D. A., & Whitworth, A. P. (2005). Binary star formation from ring fragmentation. *Astronomy amp; Astrophysics*, *437*(1), 113–125. https://doi.org/10.1051/0004-6361:20042428

Jadhav, V. V. (2025). On the detectability and parameterization of binary stars through spectral energy distributions. *Journal of Astrophysics and Astronomy*, *46*(1). https://doi.org/10.1007/s12036-025-10042-2

Jiang, I.-G., Laughlin, G., & Lin, D. N. C. (2004). On the formation of brown dwarfs. *The Astronomical Journal*, *127*(1), 455. https://doi.org/10.1086/379853

Joergens, V. (Ed.). (2014, January). *50 Years of Brown Dwarfs: From Prediction to Discovery to Forefront of Research* (Vol. 401). https://doi.org/10.1007/978-3-319-01162-2

Kaur, K. P., & Joshi, P. S. (2022). Fundamentals of differential and all-sky aperture photometry analysis for an open cluster. https://arxiv.org/abs/2209.03015

Kirkpatrick, J. (2005). New spectral types l and t. *Annual Review of Astronomy and Astrophysics*, *43*. https://doi.org/10.1146/annurev.astro.42.053102.134017

Kirkpatrick, J. (2013). Cold brown dwarfs with wise: Y dwarfs and the field mass function. *Astronomische Nachrichten*, *334*(1-2), 26–31. https://doi.org/https://doi.org/10.1002/asna.201211759

Kumar, S. S. (1962). Study of Degeneracy in Very Light Stars. *The Astronomical Journal*, *67*, 579. https://doi.org/10.1086/108658

Kumar, S. S. (1963). The Structure of Stars of Very Low Mass., *137*, 1121. https://doi.org/10.1086/147589

Kumar, S. S. (2003, June). The Bottom of the Main Sequence and Beyond: Speculations, Calculations, Observations, and Discoveries (1958–2002). In E. Martín (Ed.), *Brown dwarfs* (p. 3, Vol. 211). https://doi.org/10.48550/arXiv.astro-ph/0208096

Lang, K. R. (2013). *Essential Astrophysics*. https://doi.org/10.1007/978-3-642-35963-7

LeBlanc, F. (2010). *An Introduction to Stellar Astrophysics*.

Lomax, O., Whitworth, A. P., & Hubber, D. A. (2016). Forming isolated brown dwarfs by turbulent fragmentation. *Monthly Notices of the Royal Astronomical Society*, *458*(2), 1242–1252. https://doi.org/10.1093/mnras/stw406

Mikulášek, Z., & Krtička, J. (2005). Základy fyziky hvězd.

Oppenheimer, B. R., Kulkarni, S. R., & Stauffer, J. R. (1998). Brown dwarfs. https://arxiv.org/abs/astro-ph/9812091

Padoan, P., & Nordlund, Å. (2002). The stellar initial mass function from turbulent fragmentation. *The Astrophysical Journal*, *576*(2), 870. https://doi.org/10.1086/341790

Pecaut, M. J., & Mamajek, E. E. (2013). Intrinsic Colors, Temperatures, and Bolometric Corrections of Pre-main-sequence Stars., *208*(1), Article 9, 9. https://doi.org/10.1088/0067-0049/208/1/9

Pedagogical University of Kraków. (2022). About the observatory. Retrieved March 29, 2026, from https://www.as.up.krakow.pl/main/ginfo.php?lang=en

Pozio, F. (1991). Li in brown dwarfs and very low mass pre-MS stars., *62*, 171.

Rebolo, R., Martin, E. L., & Magazzu, A. (1992). Spectroscopy of a Brown Dwarf Candidate in the alpha Persei Open Cluster., *389*, L83. https://doi.org/10.1086/186354

Reid, I. N., & Hawley, S. L. (2005). *New light on dark stars : red dwarfs, low-mass stars, brown dwarfs*. https://doi.org/10.1007/3-540-27610-6

Reipurth, B., & Clarke, C. (2001). The formation of brown dwarfs as ejected stellar embryos. *The Astronomical Journal*, *122*(1), 432–439. https://doi.org/10.1086/321121

Skrutskie, M. F., Cutri, R. M., Stiening, R., Weinberg, M. D., Schneider, S., Carpenter, J. M., Beichman, C., Capps, R., Chester, T., Elias, J., Huchra, J., Liebert, J., Lonsdale, C., Monet, D. G., Price, S., Seitzer, P., Jarrett, T., Kirkpatrick, J. D., Gizis, J. E., . . . Wheelock, S. (2006). The Two Micron All Sky Survey (2MASS)., *131*(2), 1163–1183. https://doi.org/10.1086/498708

Stamatellos, D., Hubber, D. A., & Whitworth, A. P. (2007). Brown dwarf formation by gravitational fragmentation of massive, extended protostellar discs. *Monthly Notices of the Royal Astronomical Society: Letters*, *382*(1), L30–L34. https://doi.org/10.1111/j.1745-3933.2007.00383.x

Stellingwerf, R. F. (1978). Period determination using phase dispersion minimization., *224*, 953–960. https://doi.org/10.1086/156444

Suchan, P. (2018, October). Astronomická observatoř v ondřejově byla před 90 lety odevzdána státu. Retrieved March 29, 2026, from https://www.astro.cz/clanky/ostatni/astronomicka-observator-v-ondrejove-byla-pred-90-lety-odevzdana-statu.html

Tarter, J. (2014). Brown Is Not a Color: Introduction of the Term 'Brown Dwarf'. In V. Joergens (Ed.), *50 Years of Brown Dwarfs: From Prediction to Discovery to Forefront of Research* (pp. 19–24). Springer Publishing.

Ventura, P., & Zeppieri, A. (1998). Non instantaneous mixing: Deuterium burning in very low mass stars and brown dwarfs., *340*, 77–80.

Warner, B. D. D. (2016). *A Practical Guide to Lightcurve Photometry and Analysis*. https://doi.org/10.1007/978-3-319-32750-1

Wenger, M., Ochsenbein, F., Egret, D., Dubois, P., Bonnarel, F., Borde, S., Genova, F., Jasniewicz, G., Laloë, S., Lesteven, S., & Monier, R. (2000). The SIMBAD astronomical

database. The CDS reference database for astronomical objects., *143*, 9–22. https://doi.org/10.1051/aas:2000332

Whitworth, A. P., & Goodwin, S. (2005). The formation of brown dwarfs. *Astronomische Nachrichten*, *326*(10), 899–904. https://doi.org/10.1002/asna.200510447

Whitworth, A. P., & Stamatellos, D. (2006). The minimum mass for star formation, and the origin of binary brown dwarfs., *458*(3), 817–829. https://doi.org/10.1051/0004-6361:20065806

Whitworth, A. P., & Zinnecker, H. (2004). The formation of free-floating brown dwarves and planetary-mass objects by photo-erosion of prestellar cores., *427*, 299–306. https://doi.org/10.1051/0004-6361:20041131

Whitworth, A. P. (2018). Brown dwarf formation: Theory. https://arxiv.org/abs/1811.06833